وَمَا تَوْفِيقِي إِلَّا بِاللَّهِ، عَلَيْهِ تَوَكَّلْتُ وَإِلَيْهِ أُنِيبُ.

(صدق الله العظيم)

And my success is not but through Allah.
Upon him I have relied, and to Him I return.
(true are the words of Allah)

University of Alberta

Influence of Geomechanical Processes on Relative Permeability

by

Mohamed Tahar Hamoud

A thesis submitted to the Faculty of Graduate Studies and Research
in partial fulfillment of the requirements for the degree of

Master of Science
in
Petroleum Engineering

Department of Civil and Environmental Engineering

Fall 2012
Edmonton, Alberta

Abstract

Relative permeability curves represent an important element of special core analyses, but challenges remain in obtaining valid results and the extrapolation and use of existing permeability results is problematic. This situation is compounded in cases where core properties are altered from changes in effective stress. During the production of oil and gas reservoirs the effective stress changes as a result of changes in pore pressure or temperature. Therefore, changes in rock properties such as porosity and permeability will occur and will consequently influence reservoir performance calculations.

A series of drained triaxial compression tests were conducted to investigate the behaviour of reconstituted specimen at low stress. Subsequently, relative permeability tests were performed, under steady state process, on different levels of strain.

Our results showed that in two-phase flow, the initial oil relative permeability was more sensitive to the stress in comparison to the water one. This change was up to about 28%.

Understanding the behaviour of relative permeability at different stresses is needed to provide reliable permeability data at different states of reservoir.

Acknowledgement

I would like to express my thankfulness to my supervisor Dr. R.J.Chalaturnyk for his prompt guidance toward the achievement of this research. The acknowledgment of the author co-supervisor; Dr J.Leung is also appreciated.

Warmly esteemed to my mom who is enduring to take care toward my dad and brother who are sick and really they are in need of assistance during my absence. To my lovely wife who always provides a support and encouragement to accomplish my Masters.

The author wishes to acknowledge Foundation CMG for its financial and support this study.

A special thank you to the group of geomechanic lab; Steve, Saurav, Nathan, Ritchi, Mohammad and Gilbert for Reservoir Geomechanics Research Group, $[RG]^2$ for their help in the lab and discussions about the testing and results.

To Hope who always is smiling and responses fast through emails

Table of Contents

List of Tables

List of Figures

Nomenclature

a, b, c	Constants of Carman-Kozeny Equation
A	Cross section, m^2
A_{corr}	New area of specimen, m^2
B	Ratio of change in pore pressure to change in confining pressure
C_b	Bulk compressibility
C_{ma}	Matrix compressibility
C’	Cohesion of material
D_r	Relative density of material
e	Void ratio
f_w, f_o	Fraction of water and oil, respectively
g, g’	Gravity and centrifugal acceleration, respectively
G_w, G_s	Specific gravity of water and sand, respectively
H_o	Initial height, m
Ir	Relative injectivity
K_o	Coefficient of earth pressure at rest
$\frac{k}{k_o}$	Changes in permeability
k_{ab}	Absolute permeability, Darcy
k_{effo}, k_{effw}	Effective permeability to oil and water, respectively
k_{ro}, k_{rw}	Relative permeability to oil and water, respectively

$k_{rw}(S_{or})$	End point relative permeability to water at residual oil saturation
$k_{ro}(S_{wi})$	End point relative permeability to oil at irreducible water saturation
L	Length/height of specimen, m
M_s, M_d	Mass of saturated and dry sand, kg
n_o, n_w	Corey exponents for oil and water, respectively
N_c	Capillary number
P_f	Pore pressure
PV	Pore volume
P’	Effective mean stress, kPa
q’	Deviator stress, kPa
q_o, q_w	Flow rate of oil and water, m^3/s
q_t	Superficial velocity
r	Radius
Re	Reynolds number
S_r	Degree of saturation
S_w	Water saturation
S_{wi}	Irreducible water
S_{or}	Residual oil saturation
t	Time
v	Flooding rate

V_b, V_{bulk}	Initial volume of specimen, m^3
V_v, V_s	Volume of voids and solids, respectively
V_{pore}	Pore volume
V_{total}	Total volume
W	Water content
ϕ_{in}, ϕ_{corr}	Initial and corrected porosity, respectively
ε_a, ε_v	Axial and volumetric strain, %
ε_{xx}, ε_{yy}, ε_{zz}	Normal strain in the x, y and z-direction, respectively
σ, σ'	Total and effective stress, kPa
σ_1, σ_3	Axial and confining stress, kPa
$\sigma_{w/o}$	Interfacial tension between water and oil, mN/m
ρ_s	Density of sand
μ_w, μ_o	Viscosity of water and oil, Pa.s
ΔH	Change in height of sample, m
$\frac{\Delta P}{L}$, ΔP	Gradient of pressure and differential pressure, respectively
ΔV	Quantity of water drained out of specimen
$\Delta\rho$	Difference of density, kg/m^3
∂Pc	Capillary pressure
$\frac{\partial x}{\partial t}$	Velocity

$\frac{\partial f_w}{\partial S_w}$	Variation of water fraction
ω	Centrifuge speed, rpm
ϕ’	Friction angle
α	Poroelastic factor
θ	Angle

Chapter 1 Introduction

Nowadays, reservoir simulation takes place to understand the behaviour of flow mechanisms, such as drainage or imbibition, or wettability that are responsible for reservoir flow performance. Indeed, reservoir engineers make a great effort to perform a history match. Often, relative permeability curves are modified to obtain history match. However, during the depletion or injection of oil and gas reservoirs, the effective stress usually increases or decreases as a result of changes in pore pressure. This causes changes in rock properties such as porosity and permeability and will consequently influence reservoir management. As a result, a set of relative permeability curves sensitive to changes in effective stress, in particular shearing stress should be considered. Many researchers (Oldakowski 1994, Scott et al. 1994, Chalaturnyk 1996 and Touhidi-Baghini 1998) have investigated the behaviour of stress-strain on unconsolidated reservoirs; for instance, for the McMurray oil sands formation, Scott et al. (1994) have concluded that these kinds of reservoirs should be investigated at low stress.

1.1 Background

Initially, oil and gas reservoirs were discovered by an accident. In the 19th century, people used oil for lighting while wood and coal were used for heating and cooking as well. The economic revolution, however,

started in the 20th century when the world was in need of energy. This was lead to the discovery that from oil we can extract rich gas such as kerosene, which was used later as energy in households. Because an immense amount of this resource was received daily, people started first to ask questions about how this natural energy can cause this oil to come to the surface, then how we can store this great volume of oil and how can it be preserved for a long time. Engineers played a major role in thinking how to develop tools to extract oil on one hand and to use the science of mathematics to understand reservoir flow physics, on the other hand. Later, researchers developed equations that explained natural energy and concluded that rock properties (for instance, porosity and permeability) were the main parameters that control oil and gas reservoirs. The question that came thereafter is how to characterize these parameters in complex reservoirs. Completing the task of characterization introduced some challenges for reservoir description, such as: finding the relationship between porosity and permeability, grouping them into similar families of rock properties and introducing a concept to describe the multiphase flow system in porous media.

Numerous authors (Tiab, D. and Donaldson, E.C. 1996, Stiles, J., June24-26, 2002, Ahmed, T. 2000) have studied the characterization of petrophysical parameters from core and log data that is used in modeling

the performance of reservoirs. Results from experimental data have shown that permeability exhibits a logarithmic distribution while porosity follows a normal distribution. However, this characterization is altered by the fact that lithology may not be the same in all reservoirs and by the issue of how to upscale core plug measurements to macroscopic properties at the reservoir scale. To deal with this issue, wireline logs can be used to validate rock properties from core lab measurements, and other experiments such as grain size analysis and geologic description can also support understanding of reservoir characterization.

Afterward, authors (Honarpour, M., Koederitz, L. and Harvey, A.H., 1994) established a simple ratio that can qualitatively describe flow in porous media, commonly known as relative permeability and it defines as the ratio of the effective permeability to absolute permeability. Even though analytical techniques were developed, the most reliable approach of measuring relative permeability is experimental methods. These methods are recognized as a special core analysis in petroleum engineering. Reservoir engineers use this approach, one set of relative permeability, to simulate multiphase flow in porous media at either the production or injection stage, but questions remain as to whether the state of the reservoir can change over the primary/secondary recovery. In addition, the use of existing rock properties (porosity and permeability) results is an issue. During a history match, reservoir engineers change the

least reliable data, which are the relative permeability curves. These are typically classified and placed at the top of the hierarchy of uncertainty, so they are modified more often than other parameters, for instance, pore volume. For these reasons, however, experimental programs should be established with care to have reliable relative permeability curves prior to shearing a test specimen. Thus, it is expected that geomechanical processes will be implemented for special core analyses to support the current incorporation of geomechanics into reservoir simulation.

1.2 Research Objective

The aim of this research is to better understand the influence of geomechanical processes on relative permeability curves through porous media. The practice has been that the absolute and relative permeability data remain constant (unchanged) throughout the field life irrespective to changes in stress conditions. The hypothesis is that not will absolute permeability change but the relative permeability will change with volumetric strain. The results of this study will provide experimental data on the variation of absolute and relative permeability at different levels of strain during pre and post shearing stress on dense, reconstituted core samples.

1.3 Research Methodology

Effectively, an experimental program was set up accordingly to understand the behaviour of reconstituted samples at three low effective confining stresses of 50 kPa, 200 kPa and 600 kPa. A technique developed at the University of Alberta was used to prepare uniform dense cylindrical core samples (50.8 mm diameter and 50.8 mm height) from, as described in Chapter 3. Before and after sample preparation, weight and volumes were recorded to calculate specimen porosity. In a modified conventional triaxial setup, core samples were loaded into a triaxial cell which was connected to three syringe pumps (260D Isco). Two of the three lines were water; one of them used to maintain pore pressure and to conduct permeability tests and the second line was used to maintain cell pressure. The third line was oil used for conducting relative permeability tests. A saturation process was set to bring a sample to reservoir fluid conditions and therefore restore wettability (water-wet). Then a simple loading process was followed to restore the specimen to desired reservoir conditions. After that, absolute and relative permeability tests were performed under a steady state process and at different levels of axial strain during drained triaxial shearing of reconstituted core samples and at fixed effective stress, 600 kPa. The results from this testing are presented and described in this thesis.

1.4 Structure of Thesis

Chapter 1 describes the background of thesis, explains the objective of this research, provides research methodology and also elucidates the chronology of the thesis.

Chapter 2 presents overview of thermal processes and provides geomechanics aspect. Explains the different techniques used to conduct relative permeability curves which describe multiphase flow in porous media and includes the literature review of shear induced in two-phase flow.

Chapter 3 explains the experimental apparatus and testing procedures used in this research to examine the effect of geomechanical processes on relative permeability data at different levels of strain. These include triaxial cell, specific gravity measurement, grain size analyses, sample preparation and the procedure of lab testing of relative permeability during drained triaxial test and at pre-post shearing.

Chapter 4 presents the outcomes of rock properties for instance porosity, mineralogy and grain size, the behaviour stress-strain of synthetic sand at different effective confining stresses and the results of relative permeability curves at different levels of axial strain and at constant effective confining stress 600kPa.

Chapter 5 summarises results of this research and provides extensive recommendations for future work.

Chapter 2 Literature Review

2.1 Overview of Thermal Processes

There are six trillion barrels of heavy oil reserves deposited throughout the world. Approximately two trillion barrels are located in Alberta. Heavy oils are defined as polycyclic aromatic hydrocarbons, which consist of complex aromatic rings; they are characterized by high specific gravities 0.933 (API less than 20) and high viscosities of more than 20 poises. Their Watson factor is 10 indicating that the heavy oils are asphaltic. Because of these characteristics of the bitumen, in the past decades, enhancement in recovery techniques of heavy oil reservoirs started with a conventional thermal process to enhance the mobility of oil by injecting hot water. However, due to the rapid growth of oil consumption, especially in industry, this technique was improved by creating the most important enhanced oil recovery technology used in Alberta to extract bitumen, recognized as steam-assisted drainage commonly called SAGD. Steam assisted gravity drainage (SAGD) is based on gravity drainage flow which is an important mechanism in thermal recovery (Doscher 1966, Towson and Boberg 1967). It is an

advanced form of stimulation in which a pair of horizontal wells is drilled into a reservoir; the upper well is used for steam injection and the lower well is used as a production well. As the bitumen is heated, its viscosity reduces and is able to flow under gravity to the production well (Figure 2.1).

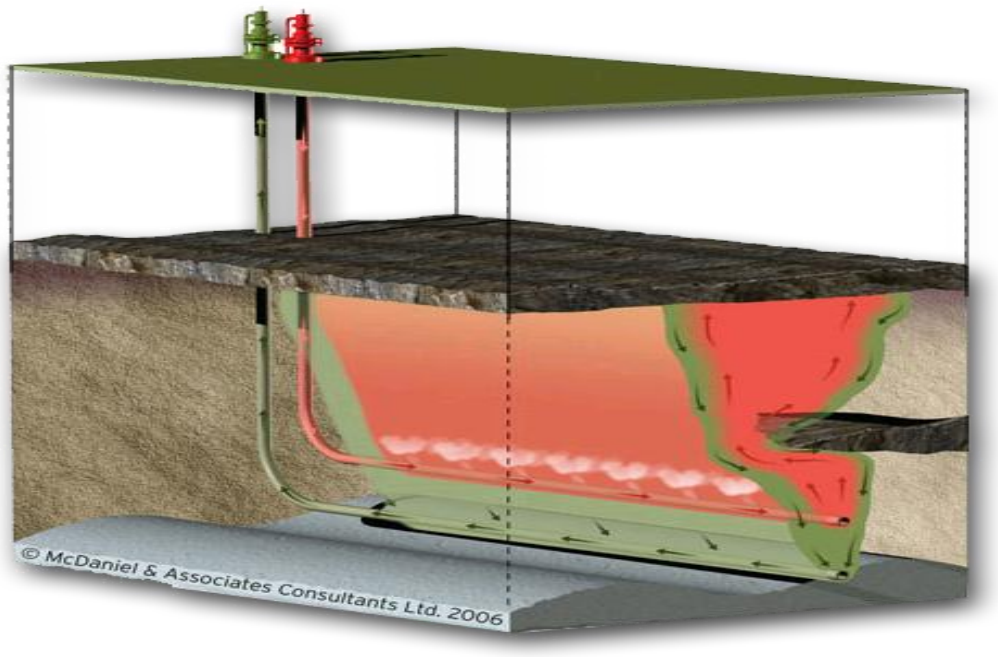

Figure 2.1: Schematic view of SAGD process.

In Alberta, bitumen is produced from shallow reservoirs. These kinds of reservoirs are unconsolidated rocks in which stress-strain behaviour is more sensitive to temperature and pore fluid pressure. The depletion or injection process often leads to a rise or reduction of the effective stress as a result of either decreasing or increasing pore pressure, respectively. This causes changes in grain arrangement or pore structure and will therefore influence reservoir engineering calculations.

Therefore, understanding of the influence of geomechanical processes on relative permeability during SAGD in unconsolidated reservoirs is important.

2.2 Geomechanics Aspect

Understanding the effect and consequence of geomechanical processes on reservoir rock properties requires knowledge of the effective stress concept, which is a fundamental parameter controlling the stress-strain behaviour of porous media. Taking into account the variation and effect of the state of stress in porous media and implementing their effects in the reservoir simulation model is essential to predict and understand, surface subsidence, which is due to reservoir compaction, or dilation due to the thermal expansion in SAGD. The consequences of geomechanics on shallow reservoirs when both pore pressure and temperature vary can lead to deformations and variations in rock properties, for instance, absolute permeability (Chalaturnyk 1996).

The principle of effective stress (Equation 2.1) is based on the theory of Karl Terzaghi (1923). The effective stress (σ') controls the matrix while the total stress (σ) controls both matrix and pore fluid pressure (P_f)

$$\sigma' = \sigma - \alpha P_f \quad \text{.....2.1}$$

where,

α : Biot factor (poroelastic factor), where $0<\alpha<1$

σ': Effective stress

σ : Total stress

P_f: Pore pressure

The Biot factor (Equation 2.2) is characterised as follows

$$\alpha = 1 - \left(\frac{C_{ma}}{C_b}\right) \quad \text{2.2}$$

where

C_{ma}: Matrix compressibility

C_b: Bulk compressibility

In unconsolidated rocks, the Biot factor (α) is close to 1. On the other hand, in hard rock (stiff frame) where the frame is incompressible compared to the compressibility of fluid, the Biot factor is less than 1 ($\alpha<1$).

In SAGD, two major geomechanical phenomena may occur: isotropic unloading and a shearing process. The first one can happen within a high pore pressure front, which can engender a reduction of effective stress and therefore an increase of permeability and porosity. However, the shearing process is predominated around the interface of drained and partially drained zones. As a result of high thermal expansion and stress, rolling or dilation of reservoir grains and rock deformation

will take place and consequently there will be variations in the petrophysics data (porosity and permeability).

The following illustration of three dimensional stresses (Figure 2.2) was developed by Poulos and Davis (1974) to assess the stress-strain relationship and therefore to know the importance of what mechanism is behind or associated with geomechanical behaviour.

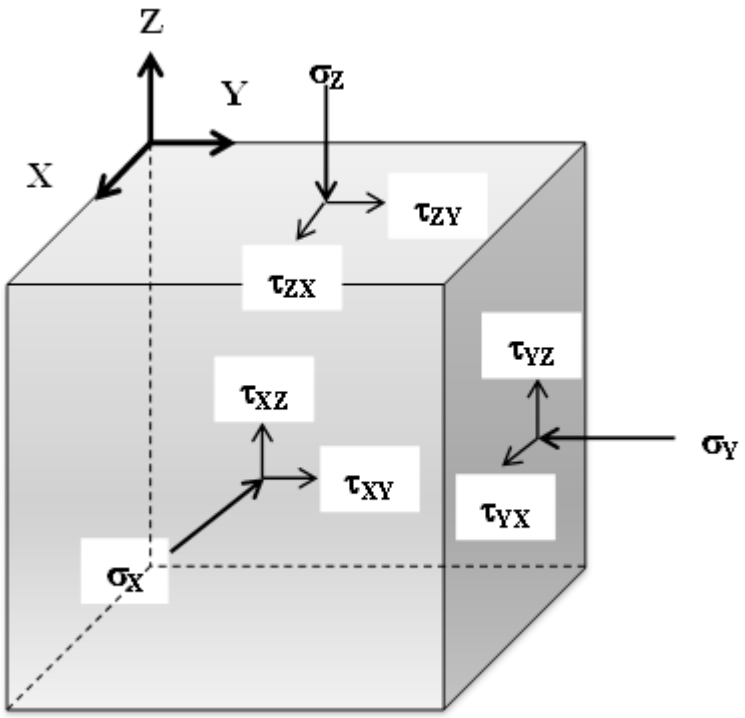

Figure 2.2: Graphical representation of three dimension stresses.

The rock matrix is sensitive to the external or internal stresses surrounding it. The deformation shown in Figure 2.3 can occur in the change of the shape of the rock matrix by either compression or extension.

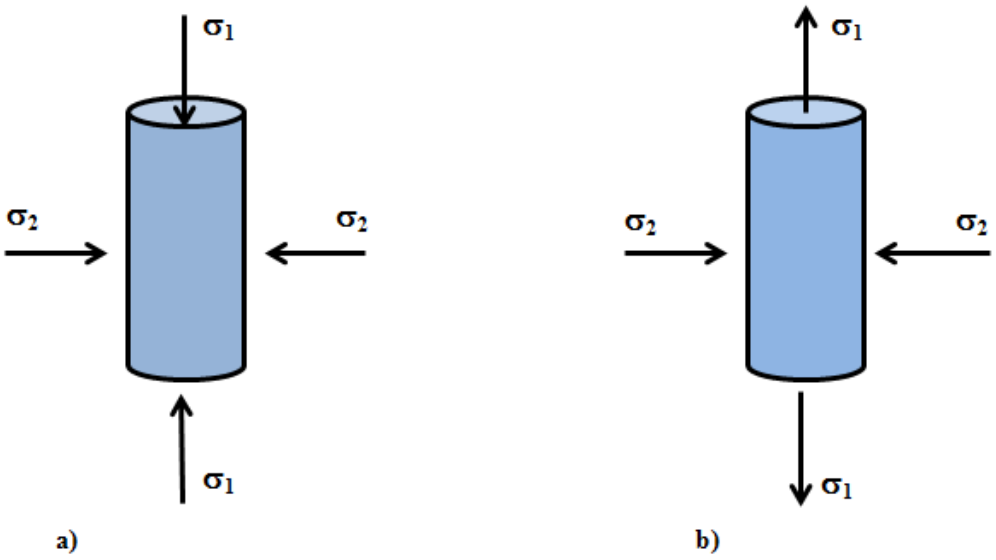

Figure 2.3: a) Compression and b) Extension view.

2.2.1Consolidated Drained Compression Test

A laboratory measurement such as the triaxial compression test is one of the most important tests that can simulate the in-situ field conditions and therefore determine rock strength parameters. It can also simulate the effect of thermal expansion during SAGD on shallow reservoirs.

As illustrated in the measurement of soil properties in the triaxial test, (Bishop and Henkel 1962), the drained test is a standard compression test, in which the specimen is first isotropically consolidated and then is subjected to shearing by rising axial stress at a constant rate and under full drainage (see detailed test procedure in Chapter 3). Simulation of the effect of thermal expansion during SAGD can be represented by the conventional loading compression stress path

(Figure 2.4), wherein the confining stress is held constant during a drained triaxial compression test and only the axial (major) stress is increased gradually.

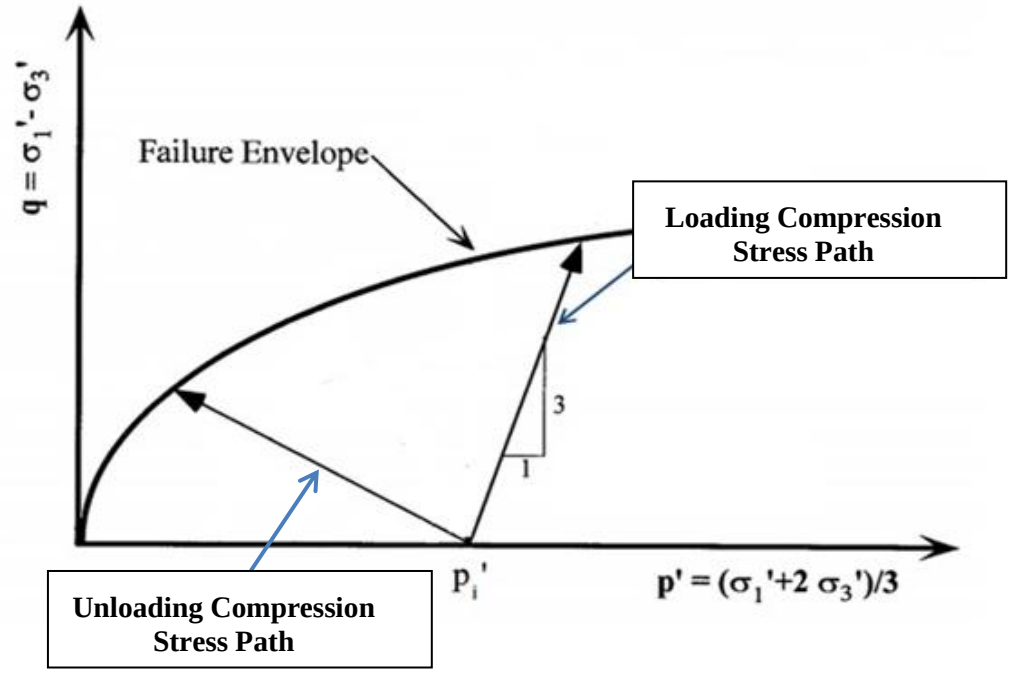

Figure 2.4: Schematic view of stress path.

Figure 2.5 shows first the growth of steam chamber due to the thermal expansion as the result of increasing pore pressure and secondly, the two major stress paths that can occur during thermal expansion.

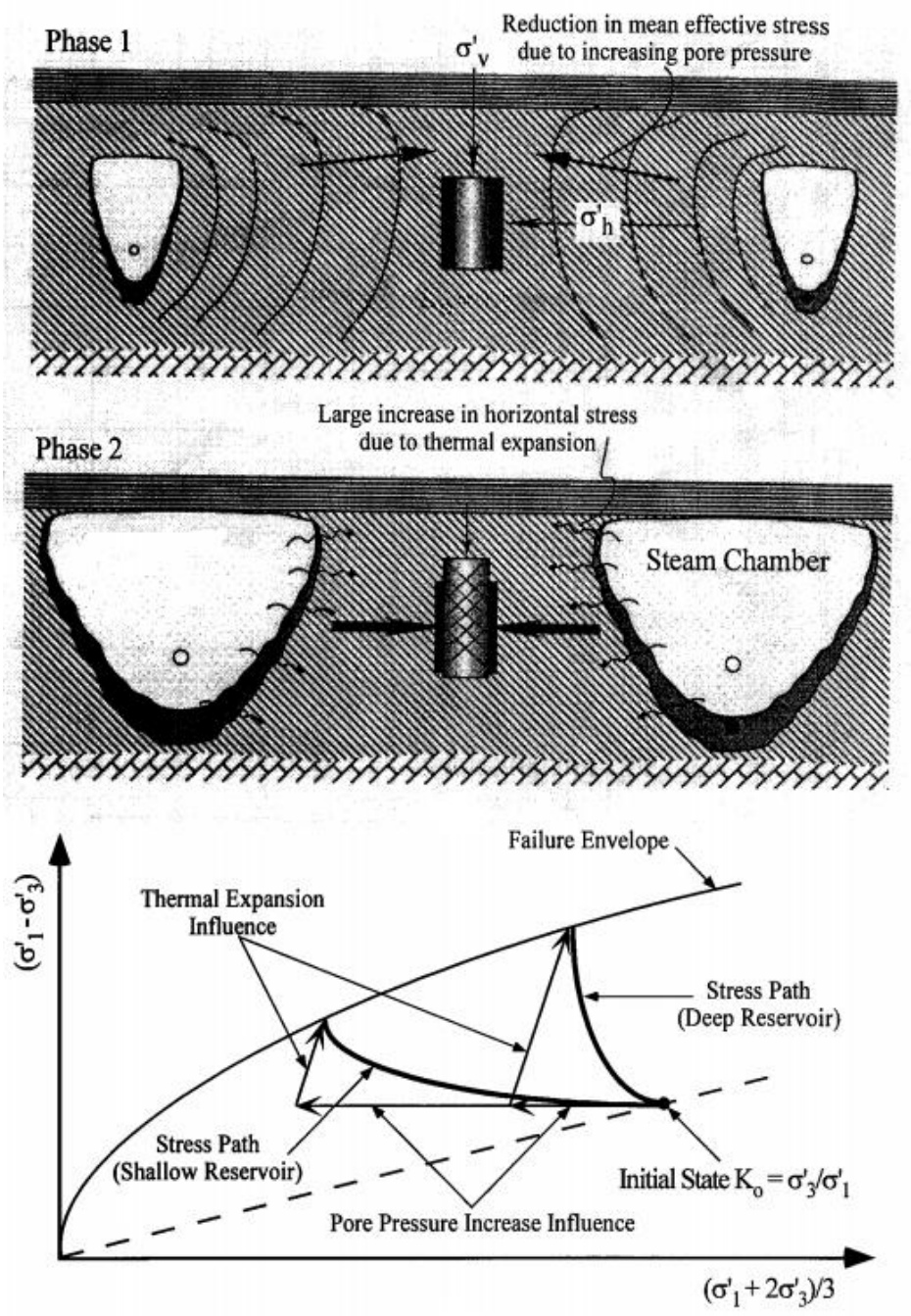

Figure 2.5: Behaviour of major stress path during SAGD

(Modified by Chalaturnyk (1996)).

2.3 Relative Permeability Measurements Techniques

In porous media, the relative permeability concept is introduced to describe multiphase flow systems. Relative permeability is defined as the ratio of the effective permeability to the absolute permeability of a porous medium. Though there are analytical statistic techniques, the most reliable approach of determining relative permeability is the experimental method. Indeed, there are three common techniques of measuring relative permeability: the steady state, unsteady state, and centrifuge methods. Each method has its advantages and disadvantages. Stiles (2002), however, ranked the steady state method as the most reliable technique for performing water oil relative permeability even though this method is time consuming. It is the method adopted in this research.

2.3.1 Steady State Technique

The steady state method is based on the concept of injection of two fluids simultaneously at various fractional flows and at either constant rates or pressure until equilibrium is reached (Figure 2.6). Flow rates and pressure gradients are recorded and used with Darcy's law to determine the effective permeability for each fluid. The advantage of the steady state method is the ability to determine relative permeability for a broad range of saturations. Based on a material balance of injected and

produced fluid and pore volume of the core sample, the average saturations are calculated.

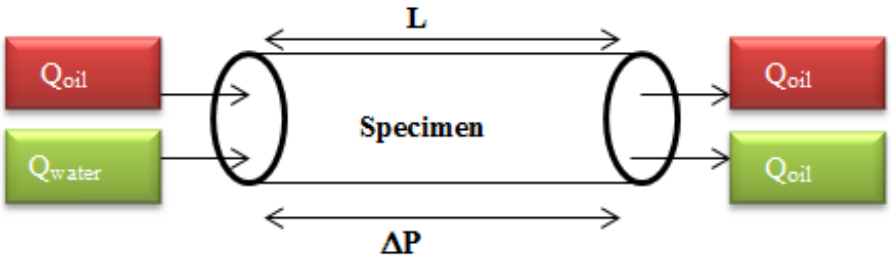

Figure 2.6: Principle of steady state process.

Theoretically, the expression of relative permeability of oil (k_{ro}) and water (k_{rw}) (Equations 2.3 and 2.4) can be written using Darcy's equation in 1D as:

Oil phase:

$$k_{ro} = \frac{\mu_o * q_o}{\frac{\Delta P}{L} * A * k_{ab}} = f(S_w) \quad \text{.....2.3}$$

and water phase:

$$k_{rw} = \frac{\mu_w * q_w}{\frac{\Delta P}{L} * A * k_{ab}} = f(S_w) \quad \text{.....2.4}$$

where; $k_{ro} = \frac{k_{effo}}{k_{ab}}$ and $k_{rw} = \frac{k_{effw}}{k_{ab}}$

k_{effo}, k_{effw}, A, μ_o, q_o, $(\Delta P/L)$, k_{ab} and S_w are the effective permeability of oil and water, cross section, viscosity of oil, oil flow rate, pressure gradient, absolute permeability and water saturation, respectively.

2.3.1.1 Advantages and Drawbacks of Steady State Technique

The advantages and disadvantages of the steady state technique are listed below:

- Define k_{rw} at low water saturation values;
- Avoid k_{rw} instability problems (unlike unsteady state method);
- Straight forward calculation; and
- Time consuming and expensive;
- Must restart if test is disturbed otherwise hysteresis effects will be introduced;
- Capillary effects; and
- Not all laboratories can conduct this method.

2.3.2 Unsteady State Technique

The concept of this method is an injection of a single phase (oil or water) to displace fluid in the core (Figure 2.7). In this technique, saturation equilibrium is not attained until the end points (if reached).

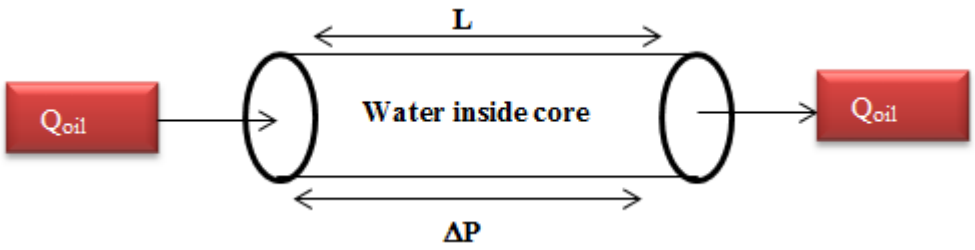

Figure 2.7: Principle of unsteady state process.

Relative permeability is derived analytically from production and pressure drop data. The most common method to determine relative permeability in an unsteady state process is the Johnson-Bossler-Naumann method (Honarpour, 1994), commonly called the JBN method. It is based on a fractional flow equation, which was developed by Buckley and Levrett (1942) and extended by Welge (1952). Equations 2.5 to 2.10 represent the development of the JBN method.

$$\left(\frac{\partial x}{\partial t}\right)_{Sw} = \frac{q_t}{\emptyset * A}\left(\frac{df_w}{dS_w}\right)_t \quad \text{.....2.5}$$

$$f_w = \frac{1+\frac{k_o}{q*\mu_o}\left(\frac{\partial P_c}{\partial x} - g*\Delta\rho*\sin\theta\right)}{1+\frac{k_o}{k_w}*\frac{\mu_w}{\mu_o}} \quad \text{.....2.6}$$

where, μ_w and μ_o are viscosity of water and oil, respectively.

f_w : represents the fraction of water;

q_t : superficial velocity;

$\Delta\rho$: difference of density between injected and produced fluids;

A: cross section;

∂P_c : capillary pressure; and

θ: angle between direction x and horizontal.

Welge (1952) suggested that the relative permeability ratio (k_{ro}/k_{rw}) can be derived from the fractional flow equation ($f_o = q_o/(q_o+q_w)$) by neglecting capillary pressure;

$$f_o = \frac{1}{1+\frac{(k_{rw}*\mu_o)}{(k_{ro}*\mu_w)}} \quad \ldots\ldots 2.7$$

However, Johnson-Bossler-Naumann provided a technique to determine individual phase relative permeability. Using Equations 2.8, 2.9 and 2.10.

$$k_{ro} = f_o \Big/ \left(\frac{d\left(\frac{1}{Q_w * I_r}\right)}{d\left(\frac{1}{Q_w}\right)} \right) \quad \ldots\ldots 2.8$$

and

$$k_{rw} = (f_w * \mu_w / f_o * \mu_o) * k_{ro} \quad \ldots\ldots 2.9$$

$$I_r = \frac{Injectivity}{Initial\ Injectivity} \quad \ldots\ldots 2.10$$

I_r: relative injectivity.

2.3.2.1 Advantages and Drawbacks of Unsteady State Technique

The advantages and disadvantages of the unsteady state technique for relative permeability measurement are listed below:

- Less time consuming and expensive;
- Many laboratories can perform it;
- Consistent with steady state results;
- It is considered as standard method;
- Flood front instability;
- No measurements of k_{ro}'s at low saturations; and
- Calculation needs to be improved.

2.3.3 Centrifuge Technique

The centrifuge relative permeability method is a fast and inexpensive process. It is based on gravity forces that dominate the flood. In this method, relative permeability to oil (k_{ro}) can be defined over a wide range of oil saturation (S_o) and can be performed on single core samples and at high temperature. Although viscous fingering is avoided in this method, the calculation of this method needs to be improved and requires validation against the results of steady and unsteady methods. A schematic view of centrifuge process is shown in (Figure 2.8).

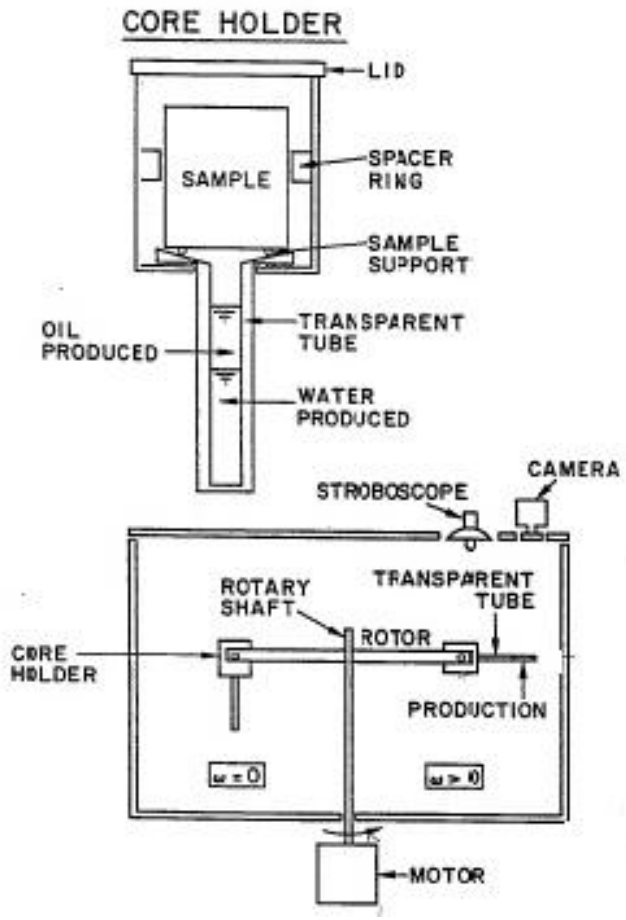

Figure 2.8: Schematic view of centrifuge process (Stiles 2002).

The determination of relative permeability from the centrifuge process is described below (Equation 2.11).

$$k_{ro} = \left(\frac{1109 * q_o * \mu_o}{k_{ab} * A * \Delta\rho * g\prime} \right) \quad \text{.....2.11}$$

where

k_{ro}: oil relative permeability, fraction

k_{ab}: absolute permeability, md

q_o: oil flow rate, ml/sec

A: area of specimen, cm^2

μ_o: oil viscosity, cp

g': centrifugal acceleration

The driving force in the centrifuge is as follows:

$g' = 0.00001117*\omega^2*r$

in which

ω: centrifuge speed, rpm and

r: radius of centrifuge arm to centre of specimen, cm.

2.4 Shear Induced Relative Permeability Literature Review

Permeability alteration due to isotropic or mean stress change has been studied by many authors. Fatt and Davis (1952) investigated this phenomenon in clean dry sandstone and at reservoir stress condition; they concluded that the changes in effective stress lead to reduction of absolute permeability. Similarly, Dobrynin (1962) studied the effect of stress on rock properties. He found an increase of confining effective stress results in a decrease of absolute permeability. In the same context, Gray and Fatt (1963) studied the effect of permeability anisotropy on different reservoir stress conditions showing that anisotropy was a function of stress. Marek (1978) observed a sharp reduction in absolute permeability under high confining pressure.

At low effective confining stress states, the variation of shear stress on permeability has also been investigated by many researchers. Scott et al. (1991) found that between a confining stress of 1 and 1.5 MPa there was an increase of 32 % of permeability during dilation stage. These results are similar to Oldakowski's (1994) and Tohidi-Baghini's (1998) work.

Fatt (1953) conducted some of the initial research on relative permeability under confining stress. He measured the gas/oil relative permeability at 20.7 MPa and found that there was not a great change in relative permeability curves at this confining pressure. Wilson (1956) followed Fatt's work by performing relative permeability measurements at different confining pressures and under simulated reservoir conditions. He found a small change in effective permeability compared to the effect of stress on absolute permeability. However, Wilson observed a small sensitivity to stress between relative and absolute permeability, which was different from Fatt's work (1953). In the same regard, other authors such as Ali et al. (1987) conducted relative permeability tests on Berea Sandstone samples under different confining stresses. They found that connate water and residual oil saturations increased with increases of effective stress and also noted that relative permeability data are more sensitive to effective stress than absolute permeability. For different types of sandstones, Jones et al. (2001) investigated the variation of relative

permeability with stress and found that the stress effects were related to rock type. Jones and Smart (2002) carried out permeability experiments with single phase and two-phase flooding during deformation and at two high fixed confining pressures. They found that the changes in the permeability of sandstone were dependent on the presence of liquid phases. Recently, Khan (2009) studied the effect of different effective stresses on relative permeability end points. He concluded there was a decrease of relative permeability end-points during compaction and an increase through dilation.

There has been no previous work performed on the influence of shear stress on relative permeability for multiple saturation states and at different levels of strain. Therefore, a major contribution of this study was to perform relative permeability measurements using the steady-state method at different levels of axial strain during drained triaxial shearing of reconstituted core samples.

Chapter 3 Experimental Apparatus and Testing Procedures

The experimental apparatus consisted of a triaxial chamber, a load frame, and three 260D Isco pumps to monitor both cell and pore fluid pressure and to conduct permeability tests. Three pressure transducers were used to measuring confining stress, pore and back pressures (inlet and outlet fluid pressure) along with other transducers for monitoring axial load, axial displacement and volume change of the specimen. Signals generated by external measurements such as transducers were connected to a data acquisition system (Datataker©**)**. Data from Isco pumps, however, were logged to LabView software. Eventually, twenty-two silica sand, uniform, dense cylindrical core samples of 50.8mm diameter and 50.8mm height; were prepared for the testing program.

3.1 Triaxial Cell

The triaxial cell used in this research was an acrylic cell and can support a maximum confining pressure of 1100 kPa. It also contains a loading ram which joins the ends of the axial load to the top pedestal. Both pedestals (top & bottom) have a diameter of 50.8 mm and a height of 50.8 mm with ports to permit drainage of pore fluids. The specimen was held between them. The test specimen is placed between the end platens and was enveloped in a latex membrane sealed with four O-rings;

two on the top and two on the bottom to prevent any pore fluid leakage from the sample. Two permeable porous stones of 50.8 mm diameter supplied by filter paper, which is characterised by medium porosity, flow rate of 60 (ml/min) and particle retention 5 to 10 micro m, both were placed on the top and bottom of the specimen respectively to stop any eventual migration of fine particles.

3.2 Load and Measurement Systems

A Wykeham Farrance load frame model was chosen for the test program. A gear driven loading system provides constant displacement rates over the range of 5.715 (mm/min) and 57.15 $x10^{-5}$ (mm/min). The load frame provides an axial load capacity of 9kN. Axial displacement was monitored using an externally mounted LVDT (Linear Voltage Displacement Transducer). The volume change of the specimen was monitored by an external volume change device, which was connected to the pore fluid pressure line (Figure 3.3). The signals generated by these transducers were recorded by Datataker. Figures 3.1 and 3.2 illustrate the configuration and elements of the testing system.

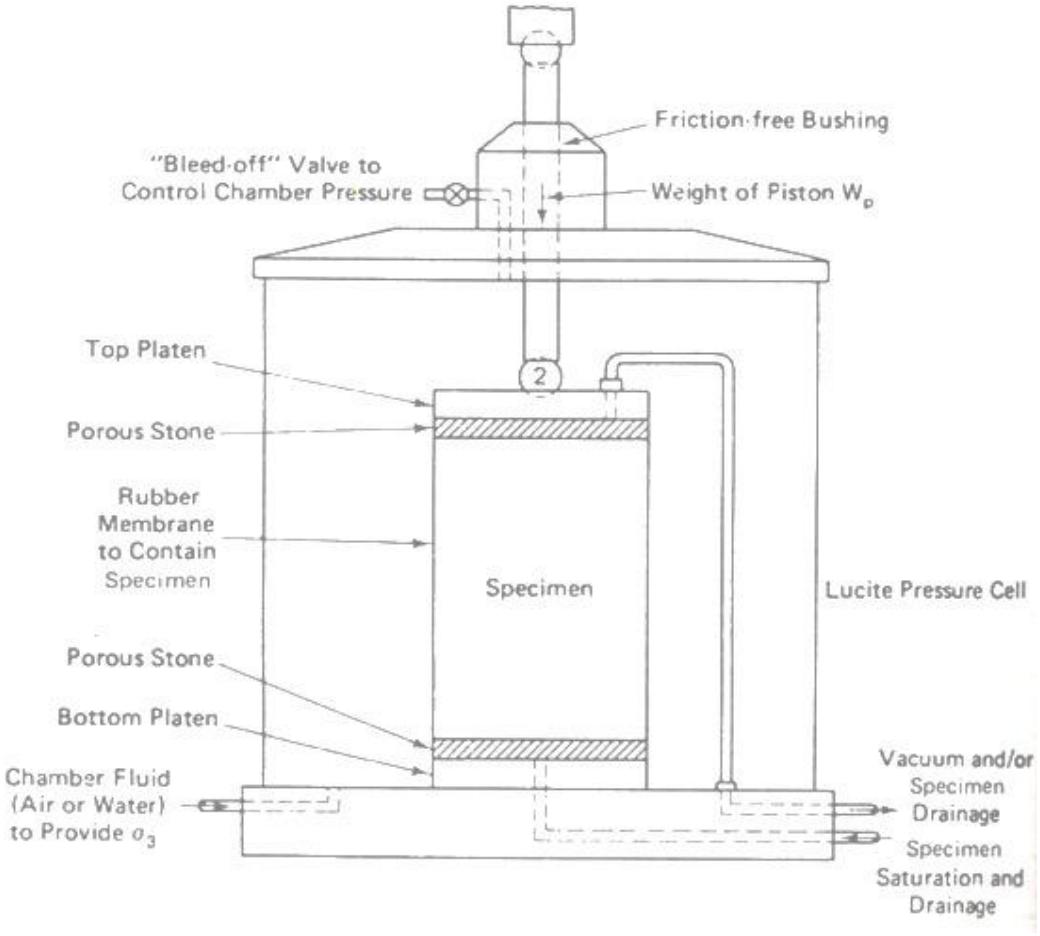

Figure 3.1: Triaxial Chamber (reference document; ASTM D 2850).

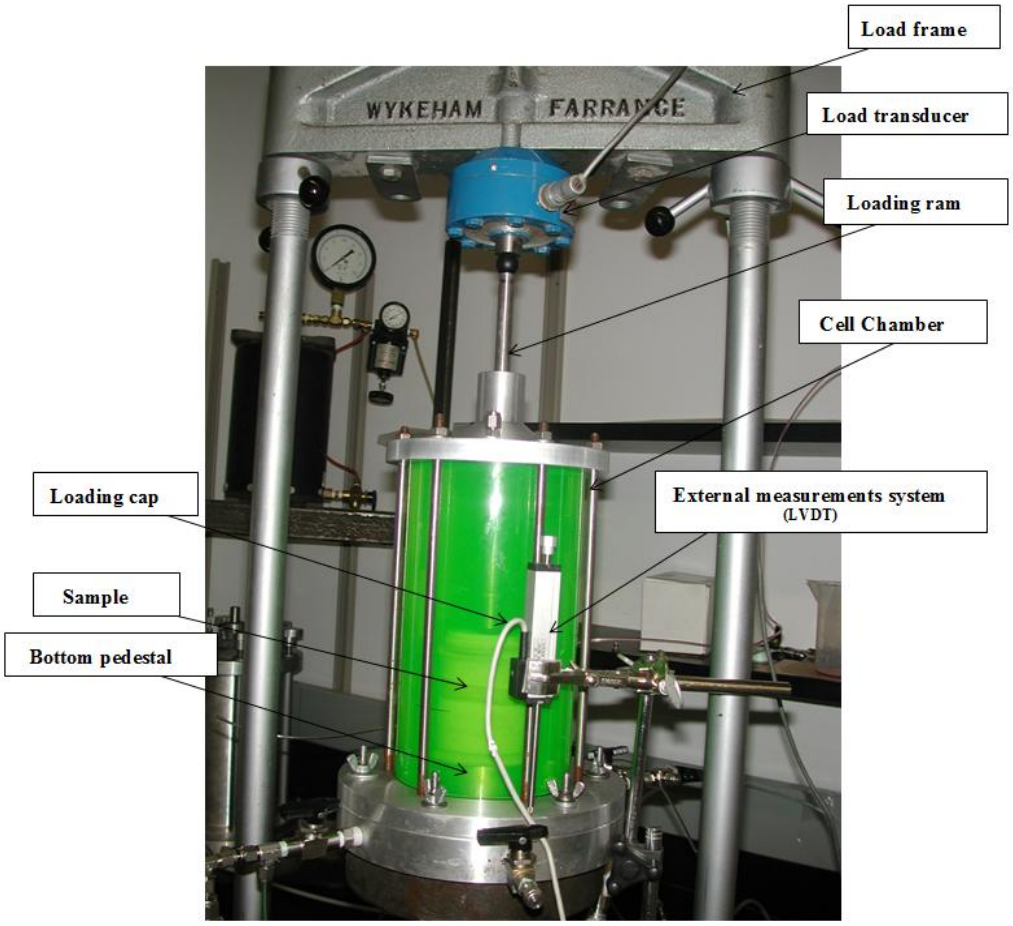

Figure 3.2: Triaxial Load Frame and cell.

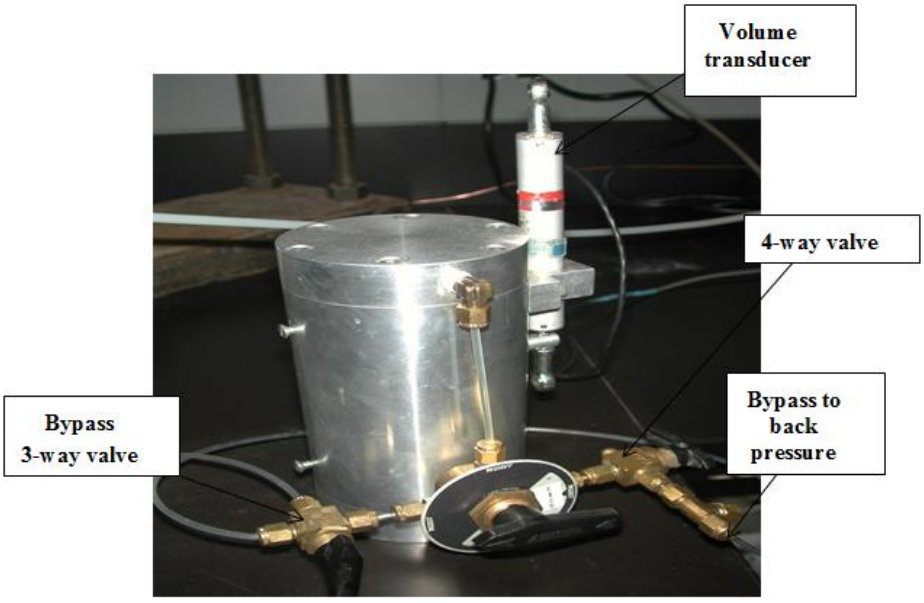

Figure 3.3: Volume change measuring device.

3.3 Measurement of Specific Gravity of Sand

Specific gravity is the ratio of sand grain density to density of water at standard conditions. The density of sand is the ratio of its mass to its volume.

3.3.1 Procedure

The following is the detailed procedure of specific gravity measurements.

a) Take a dry flask and fill it with deionised water up to the mark, measure the weight (flask + water) and temperature;
b) Throw away the water and place approximately 100 gms of sand in the flask;
c) Fill the flask 2/3 full of deionized water to submerge the sand;

d) Boil the sand+ deionized water for at least 10 minutes;

e) After boiling, handle the flask gently;

f) Cool down the flask to room temperature;

g) Check that the flask has reached room temperature (equal to step a);

h) Fill the flask with deionized water up to level and measure the weight (flask+water+sand);

i) Take a clean pan and measure its weight;

j) Pour everything (the deionized water and sand) into the empty pan;

k) Place the pan in an oven @ 110 ^{0}C to 120 ^{0}C; and

l) After 24 hours measure weight of the pan with dry sand.

3.4 Particle Size Distribution

Sieve analysis is considered one of the most important methods to determine grain size distribution from coarse to fine grain. Generally, the grain size distribution is represented by percentage of grain size passing through successive sieves of decreasing opening size.

Commonly, the sieve analysis procedure needs a motor, balance, mechanical shaker and sieves to start analyse. Figure 3.4 is a photograph of the equipment for sieve analysis. Sieve analyses were conducted in accordance with ASTM D422-63.

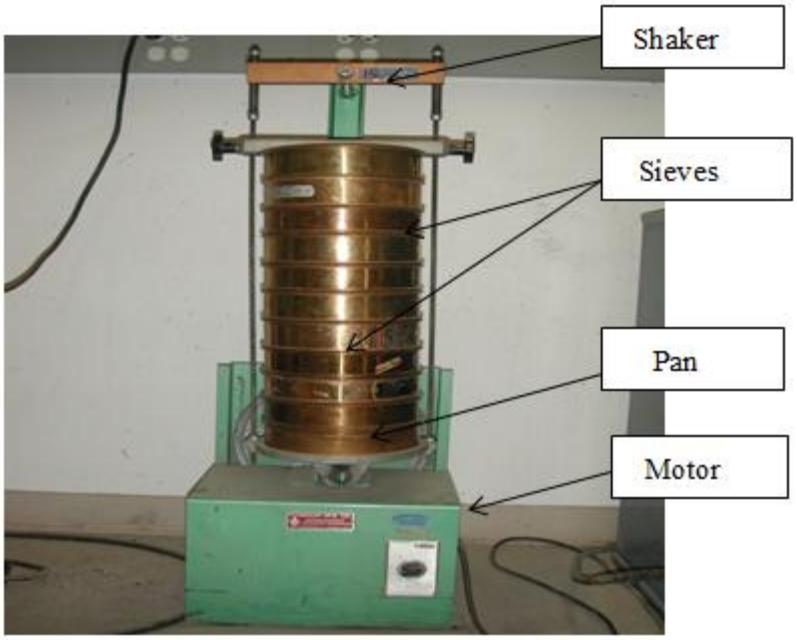

Figure 3.4: Snapshot of sieve analysis equipment.

In addition to this sieve experiment, a scanning electron microscope (SEM) analysis was performed in order to determine qualitatively the mineralogy of the sand used in this research. Relative density is a standard measure to describe the degree of compaction of a specimen. ASTM D4254 was used to determine the relative density of the test specimens.

3.5 Sample Preparation

Twenty two reconstituted sand samples were prepared from unconsolidated sand. Using a technique developed at the University of

Alberta (Manual of Artificial Oil Sand Sample Preparation, 2001). This procedure allowed multiple, nearly identical specimens to be created that permitted steady state relative permeability to be conducted at different level of strains during isotropically consolidated drained triaxial compression tests.

3.5.1 Procedure

The detailed procedure of preparing uniform dense cylindrical core samples of 50.8 mm diameter and 50.8 mm height consisted of split mold, O-rings bottom pedestal, latex membrane, top plate, top cap, cool blanket, vibration table, vacuum, porous stones (63.5 mm & 50.8 mm), water, sand and dry ice. This technique requires three stages of sand preparation, sand densification and sample freezing. The following sections describe the sample preparation procedure.

3.5.1.1 Equipment

O-rings, split mold, bottom pedestal, latex membrane, top plate, top cap, cool blanket, vibration table, vacuum, porous stones(63.5 mm &50.8 mm), water, sand and dry ice (Figure 3.5).

3.5.1.2 Sand Preparation

(a) Boil three porous stones for roughly 20 min;

(b) Weigh sand and pour water in until the beaker is half full. Boil the sand and water together for 30 minutes for the saturation purpose; and

(c) Before starting the densification, check a suitable size of the latex membrane for tiny holes (Figure 3.6).

3.5.1.3 Sand Densification

(a) Put latex membrane on the bottom pedestal and seal with O-rings. And place it on the vibrating table (Figure 3.7);

(b) Open the saturation valves, in order to remove any air, allow water to flow into the bottom of the membrane to a depth of 05 mm, and then close the valves. After that, place a 63.5 mm porous stone on the bottom pedestal. Insure that there is no air between the porous stone and the pedestal (Figure 3.8);

(c) Assemble the split mold and place it on the bottom pedestal, fold the top part of the membrane down over the mold and then seal it with O-rings (Figure 3.9);

(d) Apply a vacuum at 80 kPa from the split mold (Figure 3.10);

(e) Gradually pour the saturated sand into the membrane and start the vibration table at low speed (from 03 to 9) (Figure 3.11);

(f) Place a saturated 50.8 mm porous stone on the top and then put extra weight on the sample to apply vertical loading.

Assure that there is 2 to 3 mm of water on the top of the sample (Figure 3.12);

(g) Hold the surcharge weight vertically over the sample and turn on the vibration table to the speed of 05. This latter will come down to a desired level to produce a saturated sample (Figure 3.13);

(h) Remove the surcharge, porous stone and unfold the membrane. Again fold the membrane down over the mold and place a 63.5 mm porous stone on the sample. Fill up the mold with water (Figure 3.14);

(i) Place the top cap on top of the porous stone, let the water be pushed out of the drainage valves then close the valves. Unfold the membrane onto the top cap and seal with O-rings (Figure 3.15);

(j) Create a vacuum inside the sample. Open the split mold, place O-rings into the correct position and close the mold; and

(k) Put the top plate over the top cap and fasten it. This will avoid any uplift action during freezing (Figure 3.16).

3.5.1.4 Sample Freezing

(a) Close the bottom valves, open the top ones, and place the whole set-up into a freezing box with dry-ice for 30 minutes, make sure half the system is surrounded with dry ice;

(b) Remove the split mold and O-rings. Place a cool blanket around the frozen sand sample to maintain the temperature and thus prevent any damage (Figure 3.17);

(c) Remove both the bottom pedestal and the top cap by heating on a hot-plate just enough to remove the bottom pedestal and top cap. The sample is still attached to the porous stones on both ends (Figure 3.18);

(d) Use hot air to carefully take out the porous stones; and

(e) Remove the cool blanket and latex membrane, and keep the frozen sample in dry-ice. The sample is now ready for testing (Figure 3.19).

Figure 3.5: Sample preparation equipment

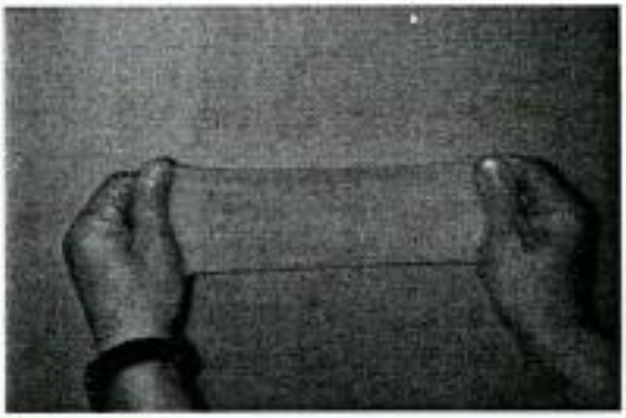

Figure 3.6: Latex membrane inspection

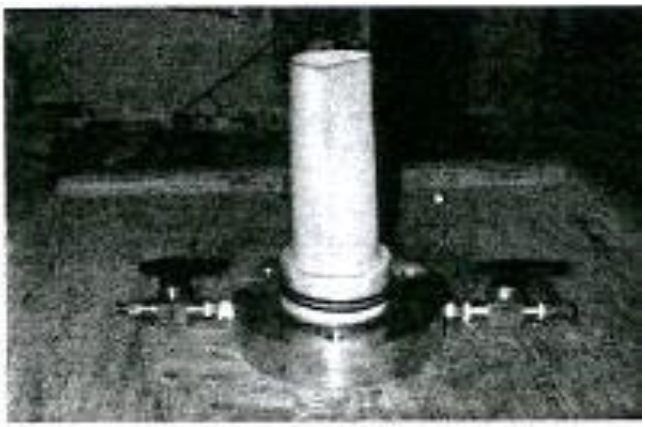

Figure 3.7: Put on the latex membrane

Figure 3.8: Saturating the bottom pedestal

Figure 3.9: Put on the split mold

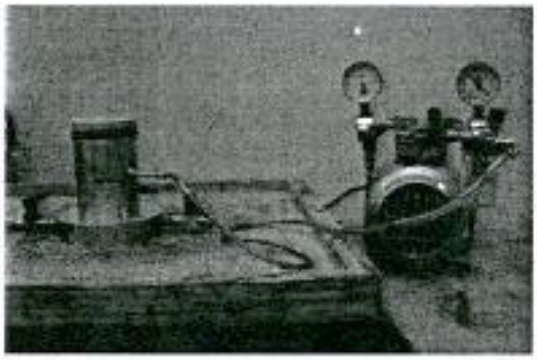

Figure 3.10: Vacuum pump connection

Figure 3.11: Scoop sand into the mold

Figure 3.12: Prepare for sand densification

Figure 3.13 : Sample densification

Figure 3.14: End of densification

Figure 3.15: Place the top cap on

Figure 3.16: Put the top plate over the top cap

Figure 3.17: Frozen sample

Figure 3.18: Remove the bottom pedestal and cap top

Figure 3.19: Synthetic sand sample

3.6 Procedure for Measuring Relative Permeability under Steady State during Isotropically Loaded Drained Triaxial Test

After having prepared uniform dense cylindrical cores samples (50.8 mm height and 50.8 mm diameter), measurements are taken to ensure both ends of samples are flat, and then their weights, dimensions and pore volumes (PV) are recorded as well as photographs taken. The detailed testing procedure is described below.

3.6.1 Triaxial Cell Preparation and Procedure

3.6.1.1 Overview

The triaxial compression test was conducted by placing a cylindrical core sample between the end platens, isolating it from the all pressure fluid by latex membrane, subjecting the core to an effective confining stress and then loading the specimen axially until failure. The cell pressure was controlled by pumping water (see Figure 3.1 and 3.2) into the cell chamber and specimen pore pressure was controlled. The volume and height of core sample varied by increasing the axial load until it reached the point of failure. This process was repeated for any additional confining stress. The cell pressure which acts equally all around the specimen is called the minor principal stress (σ_3). The applied axial load, which causes axial and radial straining within the specimen, is divided by the area of the core sample is called the axial stress. The

summation of both minor principal stress (cell pressure) and the applied axial stress is defined as major principal stress (σ_1). Consequently, the quantity (σ_1 - σ_3), called the deviatoric stress, represents the net axial stress applied to any test specimen. The volume change in the saturated test specimens is measured using the volume change device illustrated in Figure 3.3. This system measures the volume of water either entering or leaving the specimen and for saturated specimens, is a direct measure of the volumetric strain occurring within the specimen. The combination of the Datataker© system and Delogger software programs connected to a laptop were used to record all readings of volume change, cell/back pressure, axial load and vertical displacement.

3.6.1.2 Sample Mounting in Triaxial Cell

The following steps explain the detailed procedure of conducting an isotropically consolidated loaded drained triaxial compression test.

a) Saturate all drainage lines of the triaxial cell with water;
b) Place the specimen on the bottom pedestal with two saturated sintered stainless steel porous stones at both ends of the specimen;
c) Use 2 layers of 50.8 mm diameter latex membranes, and carefully place them over the specimen;

d) Pour some water on the sample and let it be held by latex membrane, in order to saturate the top drainage line;

e) Place the top pedestal on top of the specimen, and seal the specimen with two Viton O-rings on the both top and bottom pedestals. Then connect the top drainage line;

f) Assemble the top triaxial cell body with a 50.8 mm diameter loading ram;

g) Place the whole triaxial cell under a low pressure triaxial loading frame, and move the loading frame down to just above the loading ram;

h) Attach a LVDT (external measurement system) onto the loading ram to monitor the axial displacement; and

i) Saturate the confining pressure line and fill up the cell with cool fluid (Glycol and water) to keep the initial shape of the specimen. A computer-controlled positive displacement pump is used to apply the hydraulic confining pressure. Once the confining pressure system is connected, apply a desired confining pressure.

3.6.1.3 Specimen Saturation Stage

A saturation process is used to bring sample to reservoir fluid conditions.

a) Saturate all lines (pore, back and cell pressure pumps), cell and water line with water, and oil line with mineral oil. A graduated cylinder is used for receiving line. Oil and water lines are used for permeability tests (see Figure 3.1 for the schematic view of the experimental set up);

b) Apply 400 kPa of confining stress;

c) Apply vacuum pump and then flush approximately six (06) PV (pore volume) of water through the back pressure line to remove any suspected air in the system;

d) Incrementally increase cell pressure and back pressure to 600 kPa and 500 kPa; respectively and

e) Hold the system for a period of 05 days to achieve back saturation for the specimen;

f) Close the back pressure valve and conduct B test (Head, 1986);

g) Take initial pore and back/cell pressure readings;

h) Perform isotropic loading and unloading by incrementally increase (50 kPa of increment) cell pressure to a stress level of 900 kPa and decrease it down to 600 kPa.

i) Record the response of cell and pore pressure transducer readings to calculate the degree of saturation; and

j) Stop the B Test when B value becomes constant with increasing and decreasing cell pressure (Head, 1986), which provides confirmation that the specimen has reached full saturation. Figure 3.20 provides an example of the results from a B test. The B values for the test specimens used in this research are provided in Table A.1 and Figure A.1.

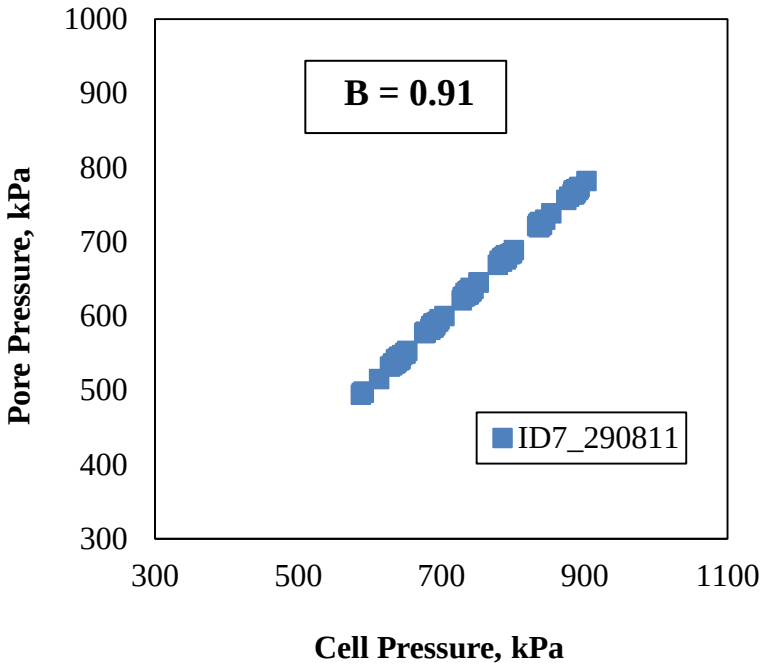

Figure 3.20: Specimen of B test. Note: The ID7_290811 corresponds to specimen 7, date of experiment August 29, 2011.

3.6.1.4 Isotropic Consolidation Stage

Isotropic consolidation (loading) process is used to bring the sample to reservoir effective stress conditions. To minimize the effect of

sample preparation freeze and thaw disturbance for these uncemented sand specimens, a seating load is needed to preserve the core sample.

a) Start loading σ' at 50 kPa; and
b) Incrementally increase cell pressure and back pressure respectively to an effective stress (σ') to 600kPa, (confining pressure greater than pore pressure); and
c) Move the ram down to make contact with the specimen.

3.6.2 Permeability Test before Shearing

It is important to measure the initial absolute permeability and relative permeability for each sample at the initial stress conditions established after consolidation of the test specimen is mandatory.

3.6.2.1 Absolute Permeability

The permeability tests were performed using the following procedure:

Measure the absolute permeability of water (k_w) by injecting water at fixed flow rate into the core; the absolute permeability is a property of the porous medium and is a measure the capacity of the medium to transmit fluids.

i. Upward flow, is initiated through the specimen at a set flow rate, until a constant differential pressure is achieved;

ii. Calculate the absolute permeability of water (k_w) using Darcy's law; and

iii. Check the value of (k_w) with repeatability test.

3.6.2.2 Steady State Relative Permeability

The steady state technique requires the capability to apply and measure fixed fractional flows of oil and water, and the resulting saturation changes. The testing procedure is described below:

i. As described above, the sample is initially saturated with of water;

ii. Inject oil into core sample in order to bring core sample to irreducible water saturation (S_{wi}), oil saturation and to permit wettability equilibrium to reach;

iii. Start the imbibition experiment, decreasing the no-wetting phase (oil) and increasing the wetting phase (water). This means injecting water and oil simultaneously at a constant flow rate mode, and monitor the differential pressure until equilibrium and steady state is achieved. Use several fractional oil/water flow rates by increasing water saturation;

iv. For fractional flow, make sure steady state conditions are obtained (the equilibrium is reached), by confirming that

flow into is equal to flow out of the specimen and then record the pressure drop, flow rates and production of water and oil at regular times;

v. Calculate the effective permeability of each fluid by Darcy's law. After that, determine the relative permeability of each phase from the ratio of the effective permeability of the phase to the absolute permeability ($k_r = k_{eff}/k_{ab}$). Then, determine the average water saturation profiles from readings of the produced water volumes;

vi. Repeat the experiment in drainage process, by increasing the non-wetting phase (oil) and decreasing the wetting phase (water). Water and oil are injected simultaneously at several increasing oil-water ratios to allow oil saturation within the core to rise; and

vii. Calculate oil and water relative permeability and determine water saturation profiles.

3.6.3 Permeability Test Pre-Post Shearing (Drained Triaxial Test)

a) Start shearing with an increase in the axial stress at low axial strain rate (0.030 mm/min);

b) At every percentage of axial strain, for example at 2% of axial strain, stop the ram, carry out the permeability tests (absolute and

relative permeability) under the steady state method, stop permeability tests, disassemble cell, put in new specimen and pass to 5% of axial strain, stop the ram, perform relative permeability test, then stop relative permeability test, etc.;

c) Start the absolute permeability test under steady state mode;

d) Perform oilflood in order to bring your specimen to irreducible water saturation;

e) Conduct relative permeability measurement with imbibition process, increasing wetting phase and decreasing no-wetting phase at first level of strain;

f) Start the desaturation of wetting phase by conducting drainage process when the final oil saturation is achieved at the end of imbibition process;

g) Record pressure drop, flow rates, water and oil productions at regular times;

h) Before going to the next strain level, a new core sample has to be loaded into cell chamber;

i) Repeat the above steps with each new strain level and perform permeability tests until the end of shearing process;

j) Once the sample attains the shearing and reaches a constant volumetric strain, stop the ram moving down;

k) Carried out the permeability test again;

l) Record pressure drop, injection and production volumes for both oil and water; and

m) Calculate oil and water relative permeability and the saturations profiles for each strain level.

Under drained triaxial compression conditions, relative permeability tests were conducted systematically after each absolute permeability test, using the steady state method, at effective confining stress of 600 kPa and at five selected strain states of 0%, 2%, 5%, 10%, and 15% covering the full range of volumetric behaviour of the specimen. These various axial strain levels were completed by using separate, nearly identical specimens. Each of these test locations is noted as red squares in Figure 3.21.

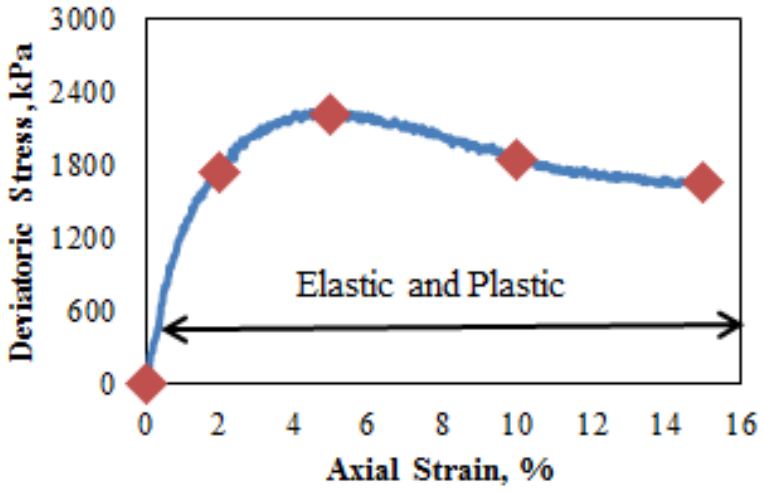

Figure 3.21: Graphical representation of five selected strain states.

The test setup used for the relative permeability experiments under steady state during the triaxial test is schematically illustrated in Figure 3.22.

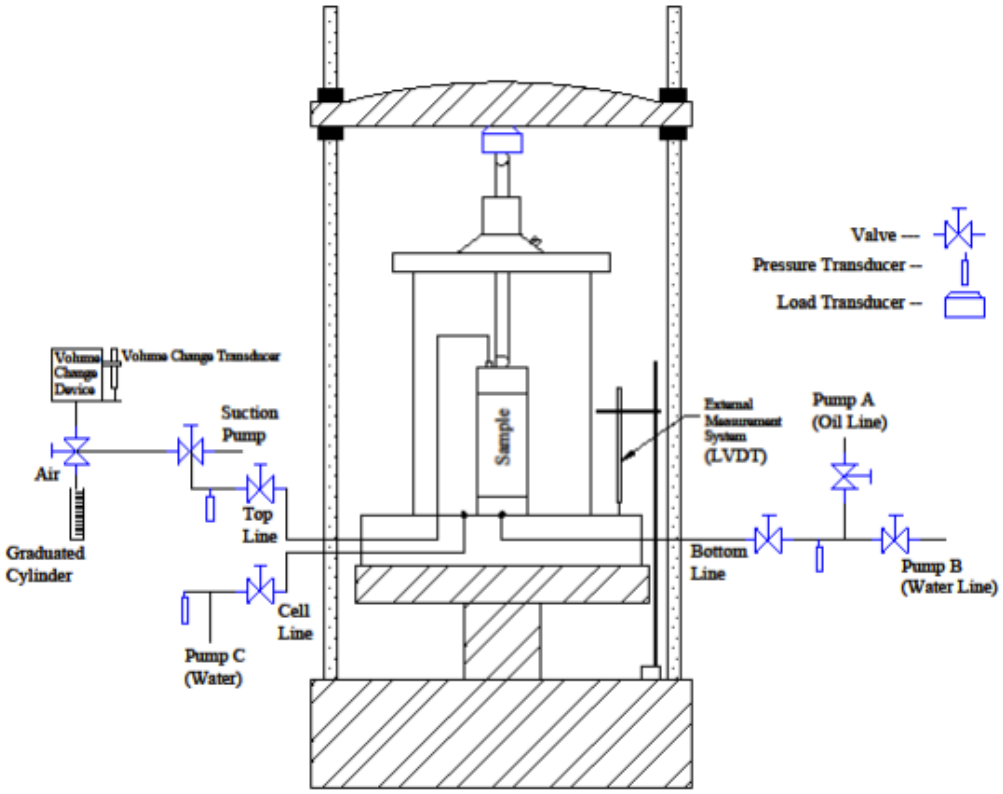

Figure 3.22: Schematic View of Experimental Setup.

3.7 Interfacial Tension Measurement (IFT)

Interfacial tension is a result of forces between two immiscible fluids which are in contact with each other. The surface which separates two fluids is under force and it creates a film layer of molecules that are in tension. The interfacial tension is expressed by force per unit length or

dynes/cm. Several methods have been developed to determine or measure interfacial tension. In this study, Interfacial duNouy Tensionmeter (ASTM D971-50), commonly referred to as the duNouy ring method, was used to measure interfacial between mineral oil and water. This tensionmeter is based on the ring method, which is equipped with circular scale to read IFT directly in dynes/cm (Figure 3.23).

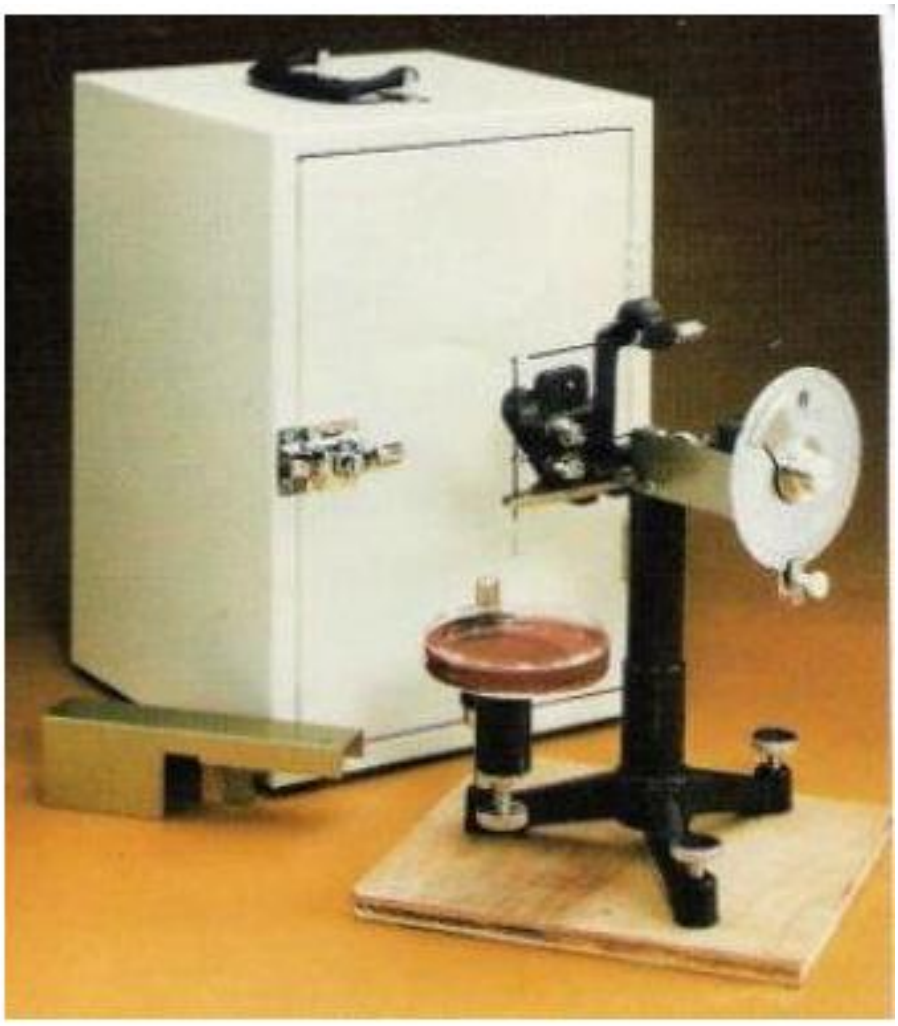

Figure 3.23: DuNouy ring, CSC Scientific DuNouy Tensiometers.

Prior measuring IFT between water and oil, a calibration step was initiated to check whether the reading of IFT is equal to the calculated IFT method (Equation3.1). Indeed, a piece of wire was used to determine its weight (M) with radius of ring (r) and acceleration force (g). The following procedure is shown below:

$IFT_{cal} = (M*g/2*r)$……3.1

M= 0.690 gr; r= 5.992 cm; g= 981 cm/s^2 and IFT_{cal} = 56.50 dynes/cm

This calculated IFT was in agreement with measured (reading) value; therefore the tensionmeter was ready for use. After this calibration step, three runs of IFT were measured (Table 3.1);

Table 3.1: Measurements of IFT between water and mineral oil

Run	Uncorrected (P) (mN/m)
1	40.8
2	44.3
3	41.9
Avg	42.33

A correction factor (F) was introduced to eliminate the effects due to the reading and to the drag of liquid on the tensionmeter ring position. This correction factor is based on ratio of the radius of the ring to the radius of curvature (r/R) which was given as 53.6, and densities of water/oil. The correction, obtained from Figure 3.24, was 1.52 (Table 3.2).

Table 3.2: Correction factor

T ^{o}c	R/r	ρ_w (D) g/cc	ρ_o (d) g/cc	P/(D-d)	Correction factor Figure 3.24 F
22	53.6	0.998	0.81	225.1773	1.52

Hence, the IFT between water and mineral oil (Figure 3.25) at room temperature (22^0C) was readjusted to 42.33 multiplied by F to give 64 (mN/m). This IFT will be essential information to check the laminar flow condition and to calculate the capillary number (Nc) in order to know whether the viscous forces or capillary forces dominate waterflood displacement (imbibition).

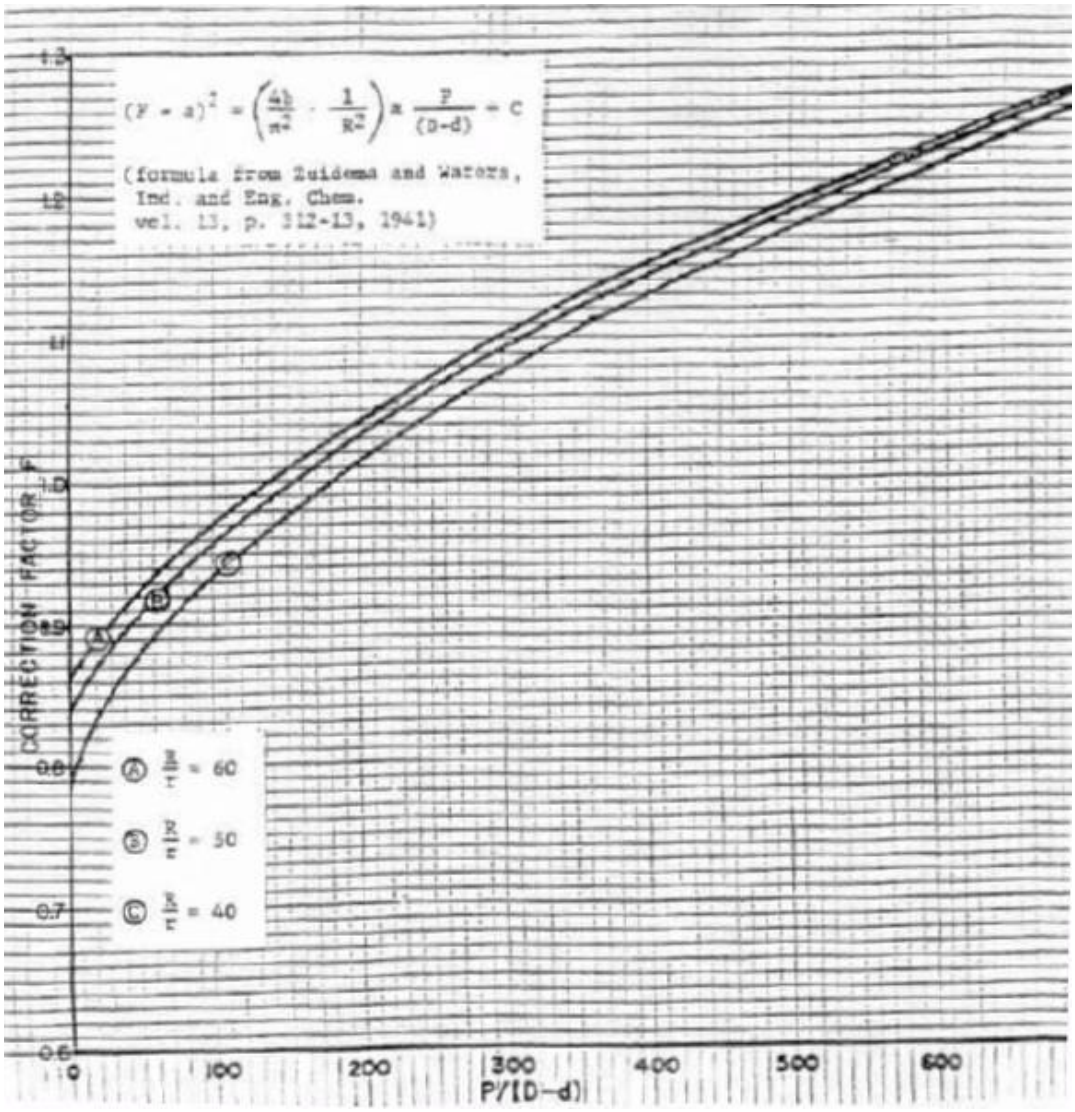

Figure 3.24: Correction factor (F) for interfacial tension (water/mineral oil), CSC Scientific DuNouy Tensiometers.

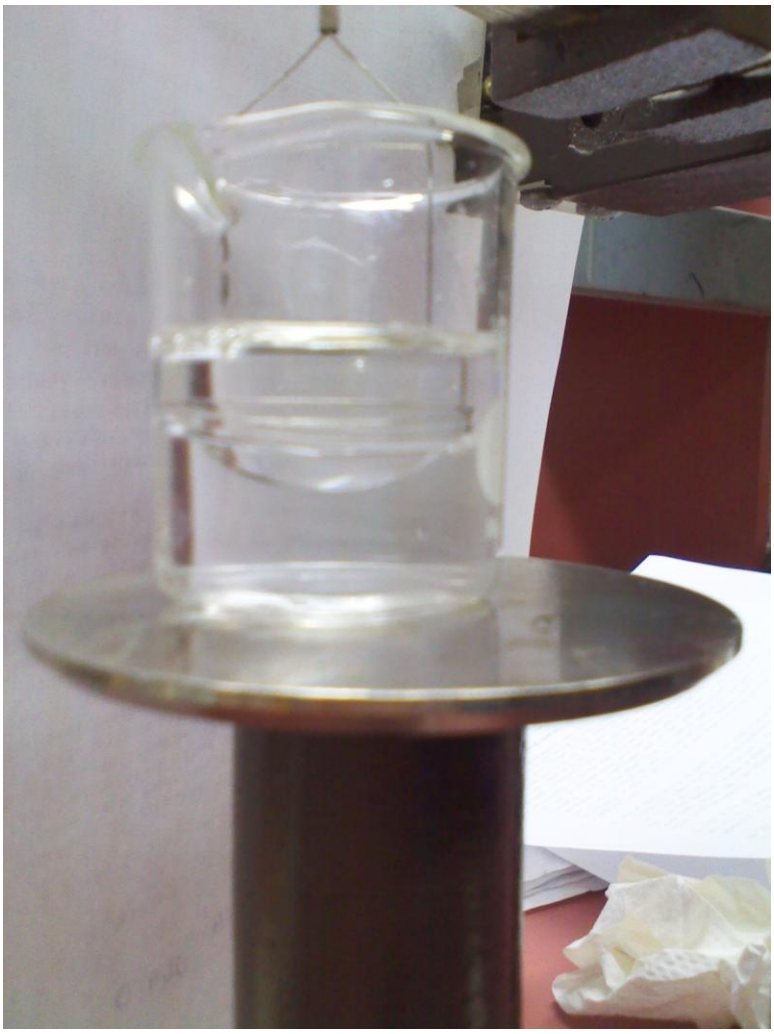

Figure 3.25: Photograph of IFT between water and mineral oil during measurements**.**

3.8 Porosity

They are many methods to determine porosity of core samples. Two of the most common porosity measuring techniques in petroleum engineering are mercury injection and gas compression/expansion. The determination of porosity of specimen is calculated as follows:

$$\phi = \frac{V_{pore}}{V_{total}} = \frac{\frac{M_s - M_d}{\rho_w}}{V_{total}} \quad \text{.....3.2}$$

where;

V_{pore}: pore volume

V_{total}: total volume

M_s: mass of saturated sand

M_d: mass of dry sand

ρ_w: water density

On the other hand, in geotechnical engineering is typically computed using moisture and specific gravity measurements and is generally expressed as a function of void ratio (e), degree of saturation (S_r), water content (W), both water (G_w) and sand specific gravity (G_s). Equations 3.3 to 3.8 describe the relationship.

$$e = \frac{Volume\ of\ voids}{Volume\ of\ solids} = \frac{V_V}{V_s} \quad \text{.....3.3}$$

$$V_v = \frac{M_s - M_d}{\rho_w} \quad \text{.....3.4}$$

$$V_s = \frac{M_d}{\rho_s} \quad \text{.....3.5}$$

and;

ρ_s: sand density

$$\phi = \frac{e}{1+e} = \frac{1}{\frac{S_r * G_W}{w * G_S}} \quad \text{.....3.6}$$

where;

$$w = \frac{Mass\ of\ water}{Mass\ of\ solids} = \frac{M_s - M_d}{M_d} \quad \text{.....3.7}$$

and,

$$S_r = \frac{w * G_s}{e * G_w} \quad \text{.....3.8}$$

In this study, the calculation of porosity was done using the geotechnical approach. It is noted that a degree of saturation (S_r) was assumed 100 % because during sample preparation, specimens were always saturated with water. Therefore, the mass of water was the difference between the mass of saturated sand (M_s) and mass of dry sand (M_d).

3.8.1 Correction of Porosity

However, this porosity was subjected to change at each level of axial strain (shear process) and therefore pore volume will eventually change. The following linear relationship porosity-volumetric strain (Equation 3.9) proposed by Li and Chalaturnyk (2003) is shown as follows:

$$\phi_{corr} = \frac{\varepsilon_v + \phi_{in}}{1 + \varepsilon_v} \quad \text{.....3.9}$$

ε_v: volumetric strain

ϕ_{in}: initial porosity before shearing

ϕ_{corr}: Corrected porosity at shearing stress

3.9 Preliminary Drained Compression Triaxial Test of Synthetic Sand

The preliminary drained triaxial compression tests for three effective stresses states of 50kPa, 200kPa and 600kPa were initiated to understand stress-strain behaviour of reconstituted dense sand sample. The experimental setup shown in Figure 3.21 and the triaxial test procedures described previously were used to perform drained tests at different effective confining stress states (50kPa, 200kPa and 600kPa).

3.10 Permeability Measurements

Absolute permeability tests were performed under steady state conditions during isotropically consolidated drained triaxial compression tests at 600 kPa effective confining stress and at different levels of strain. Steady state conditions were assumed to have been reached when flow into was equal to flow out of the specimen and when the pressure drop across the sample had stabilized at a constant flow rate of 10 ml/min. Measurements at various axial strain levels were achieved by using separate, nearly identical (i.e. initial porosity) specimens that were each strained to incrementally larger axial strains. This provides increased accuracy for absolute permeability measurements and minimizes the impact of hysteresis. Darcy's law was applied to calculate the absolute and effective permeability.

Flow was upward for the permeability testing; therefore Darcy's law becomes (Equation 3.10):

$$\boldsymbol{Q = \frac{k\,A}{\mu} * \left[\frac{\Delta P}{L} - \rho g \sin\theta\right]} \quad \text{.....3.10}$$

where,

k: permeability of core sample

μ: fluid viscosity

A: cross section of specimen

$\frac{\Delta P}{L}$: pressure gradient

ρ: fluid density

g: acceleration due to gravity

θ: inclination angle measured upward from horizontal

This final Darcy's equation form was used for determining absolute and effective permeability. However, results showed that there was a slight difference if the gravity forces were ignored, which would be the case for horizontal flow conditions.

3.10.1 Equipment

For conducting permeability tests, a two 260D Isco syringe pumps, having a capacity of 260 ml, were used to keep both water and oil flow rate constant through the system, and another 260D Isco pump was

used to apply confining stress on specimen (Figure 3.26). The Omegadyne differential pressure transducer model was chosen to measure the pressure drop across the sample. Two transducers were used to record pressure at bottom and top of sample, one transducer was placed just before inlet valve and other after outlet pore pressure valve (Figure 3.22). The other transducer was positioned before the cell valve as well. To avoid any correction of pressure readings, a simple choke was performed at the downstream flow. These transducers were connected to the laptop where the Delogger program was set to record at each desired time the pore/cell pressures, axial displacement of sample, axial load and finally specimen volume change readings. In addition to that, LabView software was also set to record the 260D Isco pumps data and from which a saturation stage was controlled at a specified time.

Figure 3.26: Snapshot of 260D Isco pumps.

3.10.2 Dead Volume

Dead volume is an extra volume remained in the conduits (connecting tubing and end-fitting) to create stacked volume. In order to have accurate average saturations, a dead volume was measured by connecting the both pedestals (top and bottom), including the two porous stones. In other words, the system was tested without specimens. Then a vacuum pump was applied for de-airing the system; after that a very low water flow rate was circulated through the system line AB and CD (Figure 3.27) to determine the final dead volume. This dead volume was monitored by one of the Isco pumps and was introduced through calculation to obtaining correct average saturation profiles. The total dead was computed to be 14.1 cm^3.

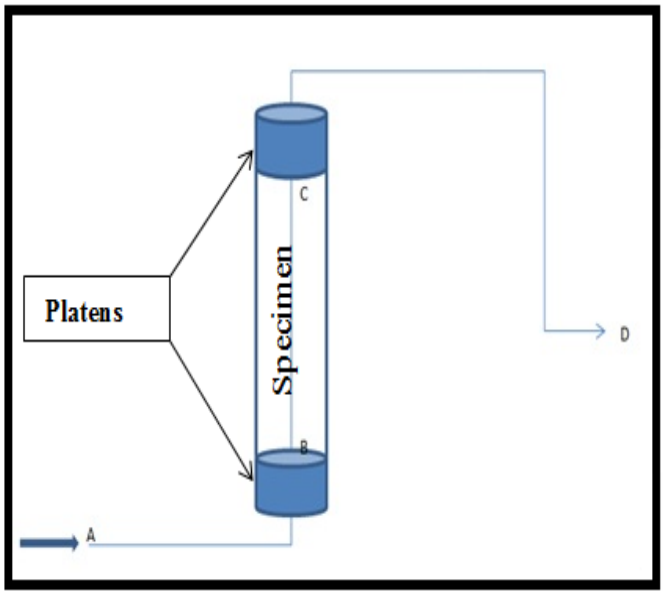

Figure 3.27: Schematic view of flow line.

3.10.3 Cross Sectional Area Correction for Specimen

During the shearing process, the cross section and height of the core sample change at each level of axial strain. These geometrical changes will impact on the permeability calculations and so a systematic correction of area and height of specimen was made for each level of strain. The area correction is related to changes in axial displacement and volumetric strain as:

$$A_{corrected} = \frac{V_b*(1-\varepsilon_V)}{H_o*(1-\varepsilon_a)} \quad \text{.....3.11}$$

where

$A_{corrected}$: new area of specimen

V_b: initial volume of specimen

H_o: initial height of core sample

ε_v: volumetric strain

ε_a: axial strain

3.11 Determination of Volumetric Strain

In the drained test, the volumetric strain (ε_v) is required to express the dilation or contraction of the sample and is determined as follows (Equations 3.12):

$$\varepsilon_v = \varepsilon_{xx} + \varepsilon_{yy} + \varepsilon_{zz} \quad \text{.....3.12}$$

where ε_{xx} represents the normal strain in the x- direction, ε_{yy} is in y-direction and ε_{zz} is in z-direction.

Regarding the volumetric strain calculation, it is convenient to monitor the expelled volume of the fluid (water) from specimen by means of volume change device, which is connected directly to pore pressure line (Figure 3.3) while a steady confining cell pressure and an increase of loading cell are constantly applied. Therefore, volumetric strain is equal to the ratio of the quantity of water drained out (or in) from the sample to initial volume of the specimen (Equation 3.13).

Hence,

$$\varepsilon_v = \frac{\Delta V}{V_b} \quad \text{.....3.13}$$

where, Δv is the difference of water volume drained out (or in) from specimen to volume change device.

Axial strain is calculated by monitoring the change in height of sample (ΔH) via an external measurement system (LVDT) and is computed using (Equation 3.14).

$$\varepsilon_a = \frac{\Delta H}{H_0} \quad \text{.....3.14}$$

where ΔH: change in height of sample

3.12 Relative Permeability Measurements

Relative permeability test (Chapter 2), the determination of the latter is the ratio of effective permeability to absolute permeability of core sample. Under the steady state method, a single phase flow conditions (water) were used to measure absolute permeability using Darcy's law to each axial strain level. After that, two-phase flow was carried out to determine effective permeability of each fluid (water and oil) using Darcy's law. Eventually, relative permeability of each phase at corresponding average saturation was calculated from the ratio of the effective permeability of the phase to the absolute permeability of the core sample.

Chapter 4 Results

After having prepared the twenty-two core samples described previously in Chapter 3, as a follow-up, sieve and SEM analyses were completed to determine the mineralogy and grain size of uncemented sand. Then, a preliminary drained triaxial compression test was performed at different effective stress states of 50 kPa, 200 kPa and 600 kPa to measure the stress-strain behaviour of the dense sand specimens at different levels of effective confining stress as well as the absolute permeability.

Eventually, at an effective confining stress of 600 kPa, a series of relative permeability tests was performed under the steady state method during an isotropically consolidated drained triaxial compression experiment and at different levels of strain.

4.1 Specimen of synthetic sand

All core samples have a similar dimension of 50.8 mm height and 50.8 mm diameter and Figure 4.1 illustrates a typical reconstituted dense sand specimen.

Figure 4.1: Dimension of specimen.

4.2 Specific Gravity of Sand Grains

Table 4.1 shows the main results obtained from the specific gravity experiments of synthetic sand.

Table 4.1: Specific gravity of synthetic sand

Sample	Method of Air Removal	$W_{(b+w+s)}$ [g]	T (^oC)	$W_{(b+w)}$ [g]	Wt. sample dry + Dish [g]	Tare Dish (empty pan) [g]	W_s [g]	α (temp. correction)	G_s
1	Boiling	740.39	21	678.13	689.51	590.36	99.15	0.9998	**2.69**
2	Boiling	735.20	21	672.44	692.45	593.27	99.18	0.9998	**2.72**
3	Boiling	734.95	21	672.34	684.40	585.13	99.27	0.9998	**2.71**

The sand chosen for this testing has an overall of specific gravity of 2.71. This specific gravity is used for determining porosity and other petrophysical parameters.

4.3 Grading and Classification of Synthetic Sand

Sieve analyses of the sand showed that the average grain size (D_{50}) of 390 µm as shown in Figure 4.2. From the particle size distribution

curve, characterization of this sand can be classified by the determination of both uniformity coefficient (C_u) and coefficient of curvature (C_c). As shown in Figure 4.2, the sand used for reconstituting the test specimens contained no fines with all particles being sand size. C_u = 1.6 and C_c= 0.72, rather than being between 1 and 3, which represents well graded sand (SW). Therefore, according to the soil classification, this synthetic sand is sorted as poorly graded sand (SP) (see Figure 4.2). These characteristics confirm that the source of synthetic sand used in this study is beach sand.

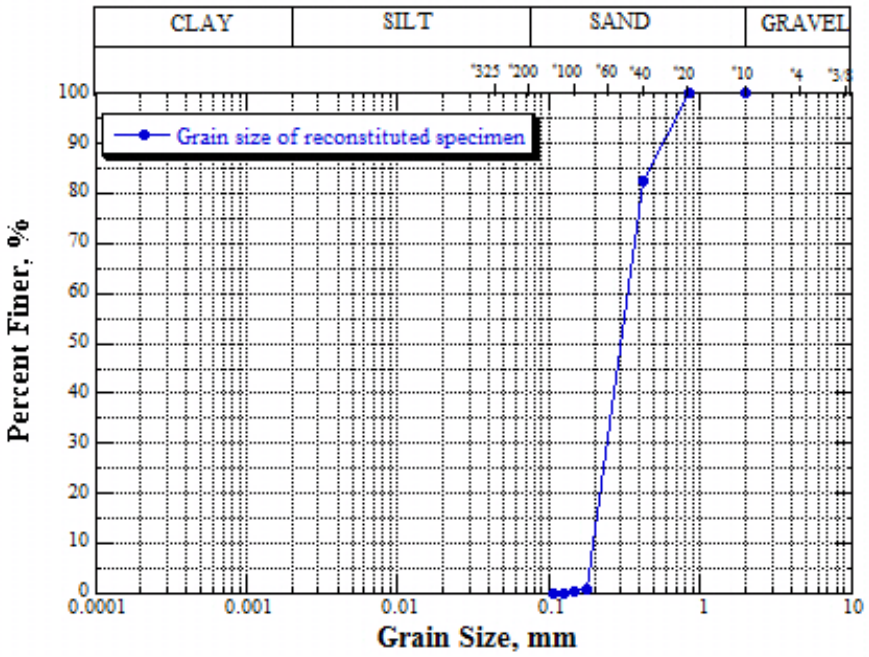

Figure 4.2: Grain size distribution curve.

A relative density (D_r) experiment also revealed that our sand can be described qualitatively as very dense (D_r>85) (Das 1999). X-ray analysis of different sections (bottom, middle and top) of the sand specimen also displayed that silica (SiO_2), which forms quartz, is the main mineralogical constituent (see Figure 4.3).

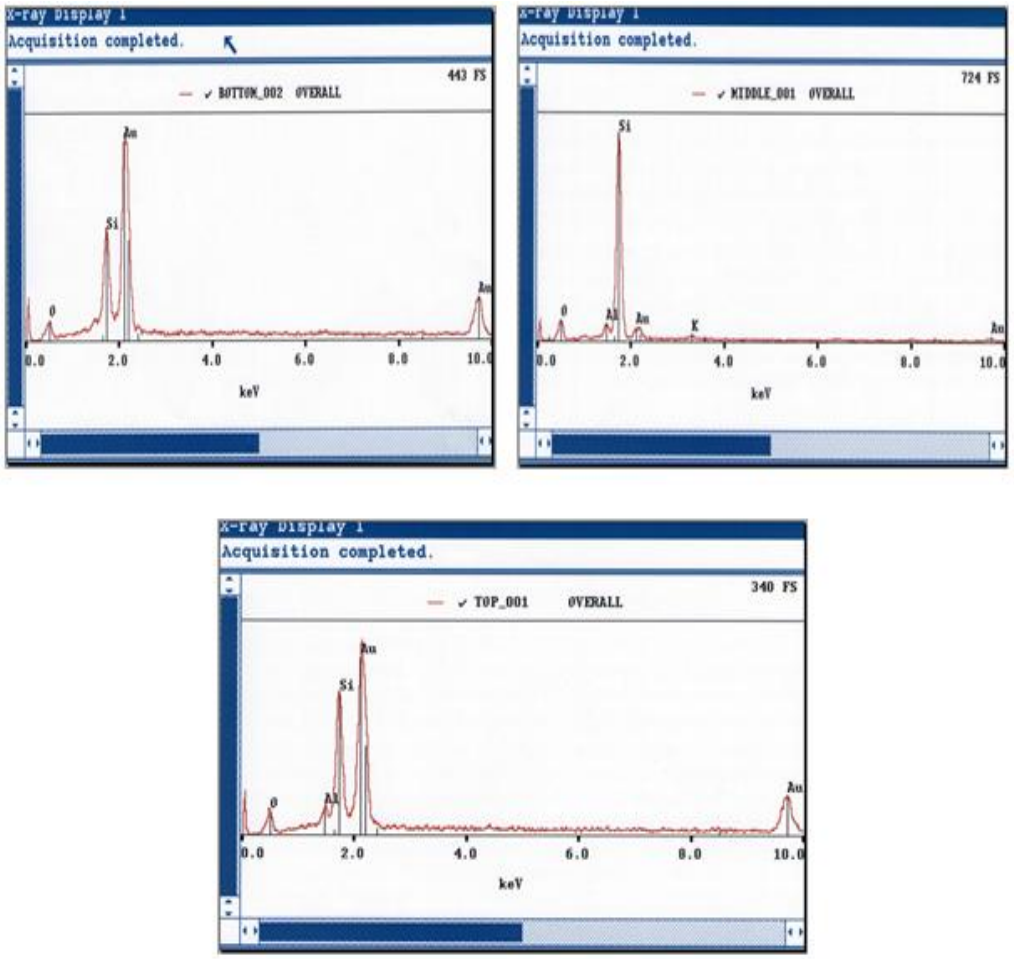

Figure 4.3: X-ray analysis of reconstituted sand.

4.4 Porosity and Other Geotechnical Parameters of Reconstituted Sand Specimen

The porosity of twenty two (22) core samples and other geotechnical parameters such as void ratio (e), and water content (W) are

summarised in the Table 4.2. The average porosity of all specimens was 34-35 %.

Table 4.2: Porosity of twenty core samples

Core Samples	Bulk Volume Vb(cc)	AirDrySand Mass(grm)	Saturated Sand Mass(grm)	Specific Gravity	Water Density (gr/cc)	Pore Volume cc	Water Content	Void ratio e	Porosity ϕ(%)
ID1_260811	102.96	178.48	213.2	2.71	1	35.54	19.45%	0.527	34.52%
ID2_260811	102.96	178.48	214.06			36.11	19.94%	0.540	35.07%
ID3_260811	102.96	178.48	213.18			35.53	19.44%	0.527	34.51%
ID4_260811	102.96	178.48	213.2			35.54	19.45%	0.527	34.52%
ID5_290811	102.96	178.48	213.76			35.92	19.77%	0.536	34.88%
ID6_290811	102.96	178.48	213.68			35.86	19.72%	0.534	34.83%
ID7_290811	102.96	178.48	213.25			35.58	19.48%	0.528	34.55%
ID8_290811	102.96	178.48	214.53			36.42	20.20%	0.547	35.37%
ID9_290811	102.96	178.48	213.77			35.92	19.77%	0.536	34.89%
ID10_290811	102.96	178.48	213.74			35.90	19.76%	0.535	34.87%
ID11_310811	102.96	178.48	213.93			36.03	19.86%	0.538	34.99%
ID12_310812	102.96	178.48	214.97			36.71	20.44%	0.554	35.65%
ID13_310811	102.96	178.48	213.5			35.74	19.62%	0.532	34.71%
ID14_310811	102.96	178.48	213.84			35.97	19.81%	0.537	34.93%
ID15_310811	102.96	178.48	213.82			35.96	19.80%	0.537	34.92%
ID16_310811	102.96	178.48	213.84			35.97	19.81%	0.537	34.93%
ID17_010912	102.96	178.48	214.18			36.19	20.00%	0.542	35.15%
ID18_010911	102.96	178.48	213.54			35.77	19.64%	0.532	34.74%
ID19_010911	102.96	178.48	213.54			35.77	19.64%	0.532	34.74%
ID20_010912	102.96	178.48	213.48			35.73	19.61%	0.531	34.70%
ID21_010911	102.96	178.48	213.93			36.03	19.86%	0.538	34.99%
ID22_010911	102.96	178.48	213.55			35.78	19.65%	0.532	34.75%

4.4.1 Permeability-Porosity Relationships of Sand Specimen

In this section, the permeability-porosity relationships are analyzed and presented qualitatively. The most popular correlations to estimate permeability in a homogenous and uniform reservoir are Carman-Kozeny (1937), Wylie et al. (1950) and Timur (1968). The first attempt was to fit experimental data of permeability with Kozeny-Carman equation. Reassuringly, a permeability-porosity relationship of

synthetic sand shown in Figure 4.4 and Equation 4.1 is similar to the Polikar et al. (1988) results.

$$k = \mathbf{0.149} * \frac{\phi^3}{(\mathbf{100}-\phi)^2} \quad \text{.....4.1}$$

where, k is in μm^2 and ϕ in %

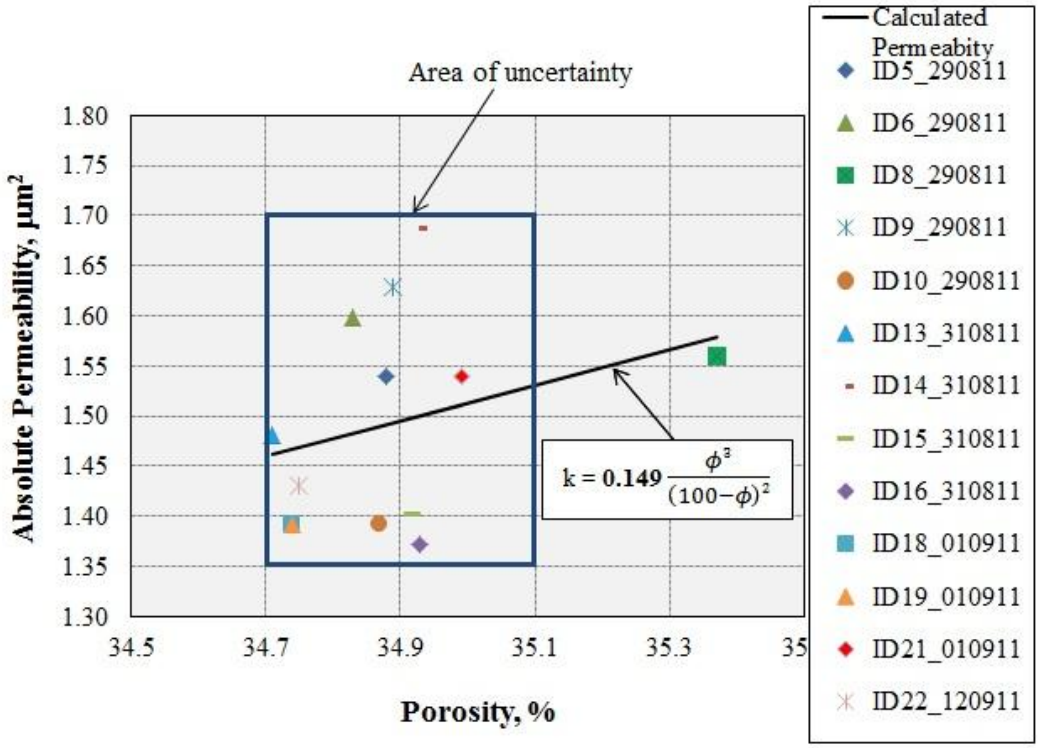

Figure 4.4: Permeability-porosity relationships of synthetic sand. Legend code: ID5_290811 means specimen #5 and August 29, 2011 date of the test.

Subsequently, a nonlinear least-square curve fitting was initiated to find the coefficients of each equation that fit the laboratory data. Using the data shown in the region (area) in Figure 4.4, the accuracy for absolute permeability (k_{ab}) measurements has computed to be +/- 0.20

Darcy. Figure 4.5 shows that it was possible to develop a reasonable qualitative prediction of the absolute permeability of uniform dense sand.

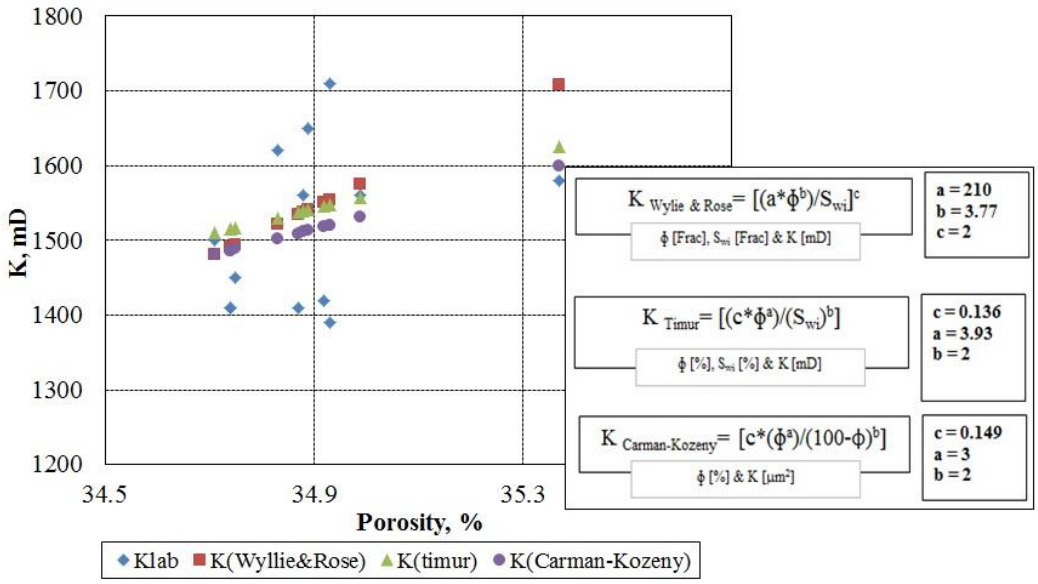

Figure 4.5: Estimation of permeability from empirical correlations.

4.5 Behaviour of Specimen during Triaxial Compression at Effective Confining Stresses of 50, 200 & 600 kPa

4.5.1 Stress-Strain

The preliminary drained triaxial compression test results at three effective confining stresses of 50 kPa, 200 kPa and 600 kPa are shown in Figure 4.6. The results show classic expected behaviour for dense, uncemented sands where, for increasing effective confining stress, stiffness increases, the deviator stress at failure increases and the volumetric strain decreases. Confirmation is also indicated by relative

density (D_r>85) results. Indeed, the deviator stress increases gradually to reach peak value which represents an elastic limit and then declines to become constant as axial strain increases, displaying the typical strain softening response for dense sand specimens.

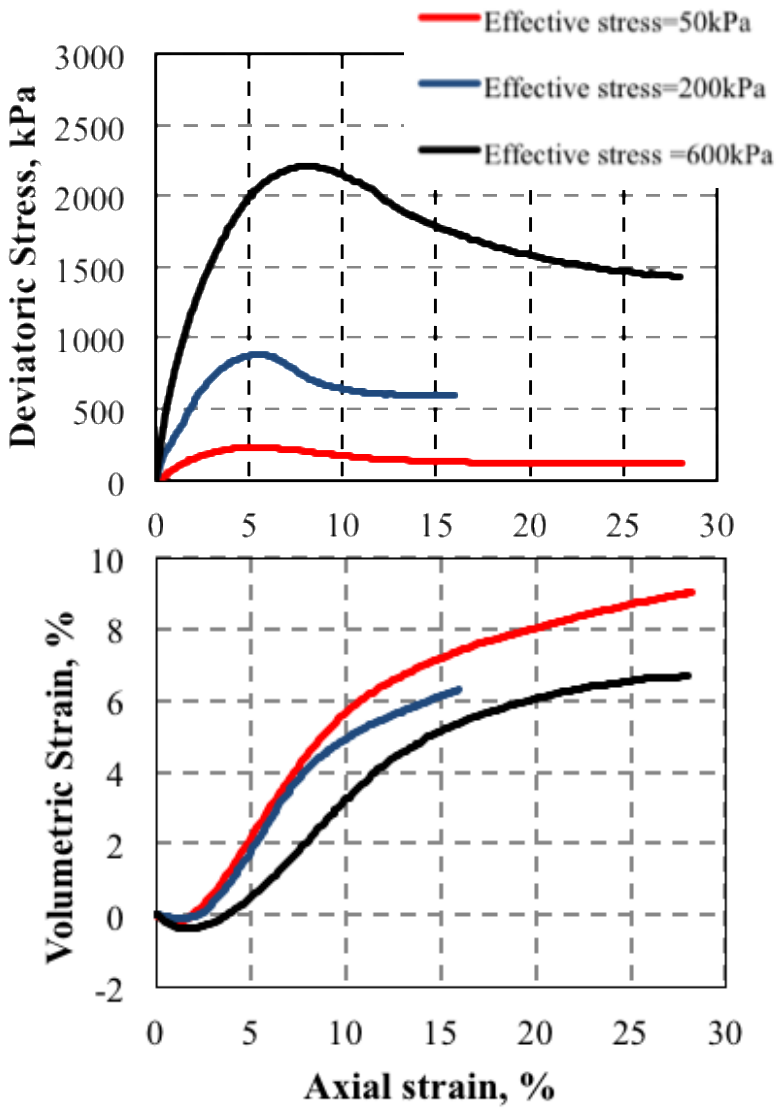

Figure 4.6: Stress-axial strain-volumetric strain of specimens at different effective confining stresses of 50kPa, 200kPa and 600kPa.

Young modulus values of 8600 kPa, 34000 kPa, and 90000 kPa were obtained for effective confining stresses of 50 kPa, 200kPa, and 600 kPa respectively, indicating that there is an increase in the degree of stiffness of the core sample as confining stress increases. Young modulus (stiffness) values of 8.6 MPa, 34 MPa and 90 MPa computed at an axial strain of 0.25%, were obtained for effective confining stresses of 50 kPa, 200kPa, and 600 kPa respectively (Figure 4.7).

The axial strain at failure (on peak stress) for these reconstituted sand specimens ranged from 5 to 6%, which is in agreement with the literature (Arora 2005). Table 4.3 summaries the deviator stress, axial strain and volumetric strain at failure. Further details of the test results are shown in Figures A2 through A7 in the Appendix.

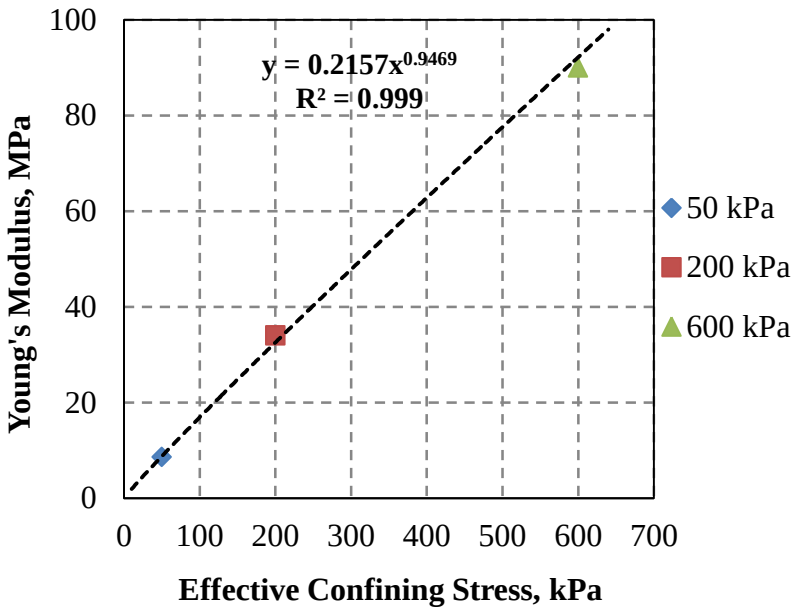

Figure 4.7: Variation in stiffness with effective confining stress.

Table 4.3: Summary of stress-strain at failure and at three effective stresses 50kPa, 200kPa and 600kPa.

Effective stress=50kPa			Effective stress=200kPa			Effective stress =600kPa		
Deviatoric Stress kPa	Axial Strain %	VoL Strain %	Deviatoric Stress kPa	Axial Strain %	VoL Strain %	Deviatoric Stress kPa	Axial Strain %	VoL Strain %
235	**5.5**	**3.4**	**879**	**5.5**	**2.2**	**2322**	**6.1**	**2.4**

4.5.2 Mohr Coulomb Failure (Strength) Envelope

The stress path followed for each of the three test specimens is illustrated in Figure 4.8. The stress path plots use mean effective stress and shear stress as the x and y variables, which means the paths are tracking the tops of the Mohr circles as the test progresses. Knowing that sand is a cohesionless material (c'=0), the friction angle ϕ', can be obtained by computing the slope of line connecting the peak of each stress path and using the geometrical relationship $\tan\alpha = \sin\phi'$, $\phi' = 34^0$ is computed for the dense sand specimens used in this research.

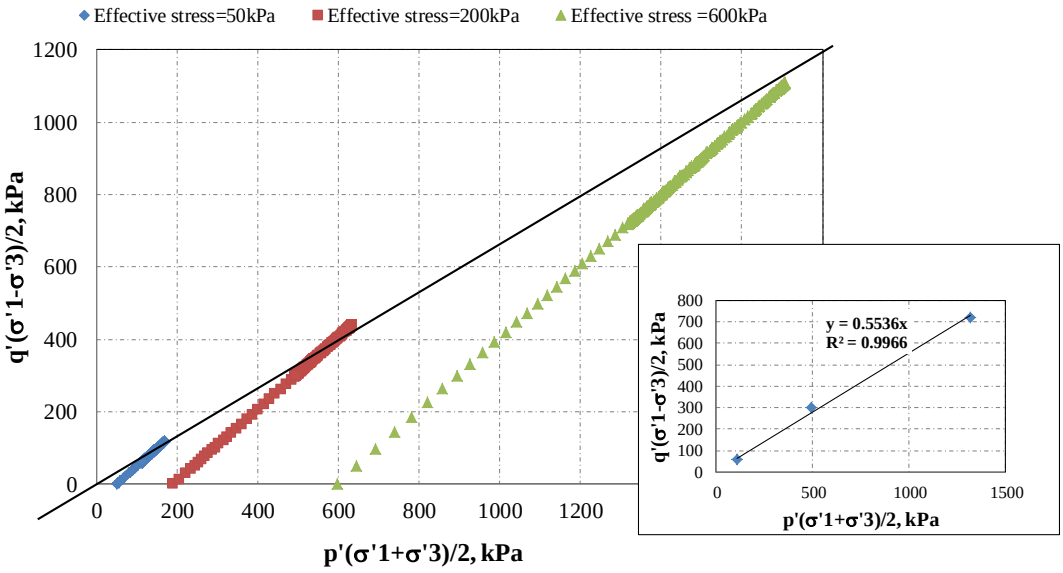

Figure 4.8: q'-p plot of three effective stresses, 50 kPa, 200 kPa and 600 kPa of synthetic sand.

4.6 Absolute and Relative Permeability at effective Confining Stress of 600 kPa

The main results obtained from absolute and relative permeability tests during the triaxial compression test at an effective confining stress of 600 kPa is presented below.

4.6.1 Absolute Permeability

Prior to performing absolute permeability measurements, a quality check was conducted to control the stabilization criteria for instance, quality check, flood steadiness and flow regime and determine the optimum of flow rate as well.

4.6.1.1 Capillary Number

In the context of checking whether the capillary forces or viscous forces dominate waterflood displacement, the capillary number (N_c), which is the ratio of the viscous forces to the capillary forces, was calculated from the following Equation 4.2:

$$N_c = (Q_w/A)*(\frac{\mu_w}{\emptyset*\sigma_{w/o}}) \quad \text{.....4.2}$$

where Q_w, μ_w, $\sigma_{w/o}$, A and ϕ are water flow rate, water viscosity, interfacial tension (IFT) between water and oil, cross section and porosity of specimen, respectively.

The capillary number for a waterflood, which was used in permeability test at room temperature, varied from 1 E-06 to approximately 4 E-06, as summarized in Table 4.4. Therefore, according to Foster (1973) and Melrose et al. (1974), the capillary forces dominate the flow process.

4.6.1.2 Scaling Factor

The scaling factor ($Lv\mu_w$), which combines the effects of core length, flooding rate and water viscosity, proposed by Rapoport et al. (1953) in order to check the stability of flood was within the tolerable range 0.75 to 2.5. Table 4.4 summarizes the results for capillary number, IFT, flow regime and the scaling coefficients at different flow rates.

Table 4.4: Summary of IFT, capillary number, scaling factor and flow regime as a function of flow rate and at room temperature

Q_w cc/min	IFT (w/o) mN/m	Capillary Number N_c	Scaling Factor $Lv\mu_w$ cm^2cp/min	Flow Regime Check Re
3	64	1.11E-06	0.75	0.007
5	64	1.85E-06	1.25	0.012
7	64	2.59E-06	1.75	0.017
10	64	3.71E-06	2.51	0.025

Following the quality control tests, an absolute permeability test was performed at the steady state method during an isotropically loaded drained triaxial compression experiment, and at different levels of axial strain, for an effective confining stress of 600 kPa. Table 4.5 and Figure 4.9 below show the variation of absolute permeability during compaction and dilation.

It is noted that the flow regime during waterflood was laminar flow and the Reynolds number (Re) was less than 1; this was in agreement with condition of laminar flow in porous media (**Re<<1**) (see Table 4.4).

The variation of absolute permeability shown in Figure 4.9 clearly decreased during compaction, reaching approximately 67% below its initial average value (1.5 D) at 5% of axial strain, and increased during dilation, attaining an increase of nearly 33% at the end of the test compared to its initial average value (see Table 4.5 and Figures 4.9

and 4.10). The initial permeability reduction occurred due to the initial compaction of the grain matrix, followed by a post-peak improvement of permeability resulting from the dilatant re-arrangement of grains and increase in porosity. These variations of absolute permeability during compaction and dilation have been shown by many authors such as Oldakowski (1994), Touhidi (1998) and Yaich (2008).

Table 4.5: Permeability-Porosity versus axial strain of synthetic sand at an effective confining stress of 600 kPa

Axial Strain %	Volumetric Strain %	Absolute Permeability D	Porosity Frac	Normalized Permeability
0	0.00	1.50	0.3475	1.00
2	-0.41	1.00	0.3448	0.67
3	-0.27	0.66	0.3457	0.44
5	0.44	0.50	0.3503	0.33
9	2.62	0.52	0.3642	0.35
11	3.68	0.59	0.3707	0.39
15	5.10	1.06	0.3792	0.71
20	6.02	1.99	0.3846	1.33

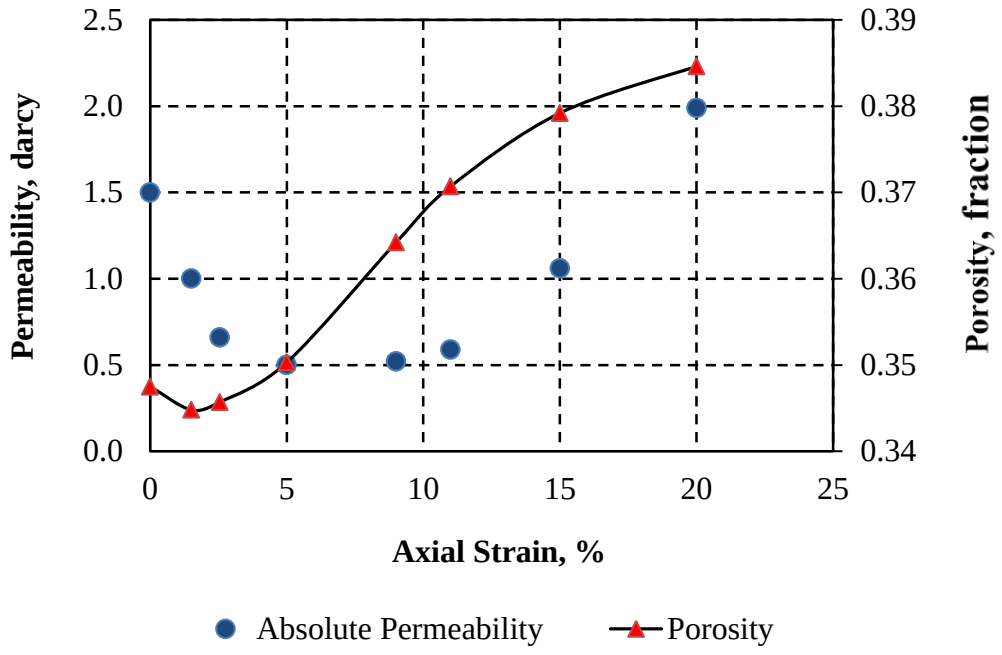

Figure 4.9: Absolute permeability and porosity versus axial strain test of a specimen at an effective stress of 600 kPa.

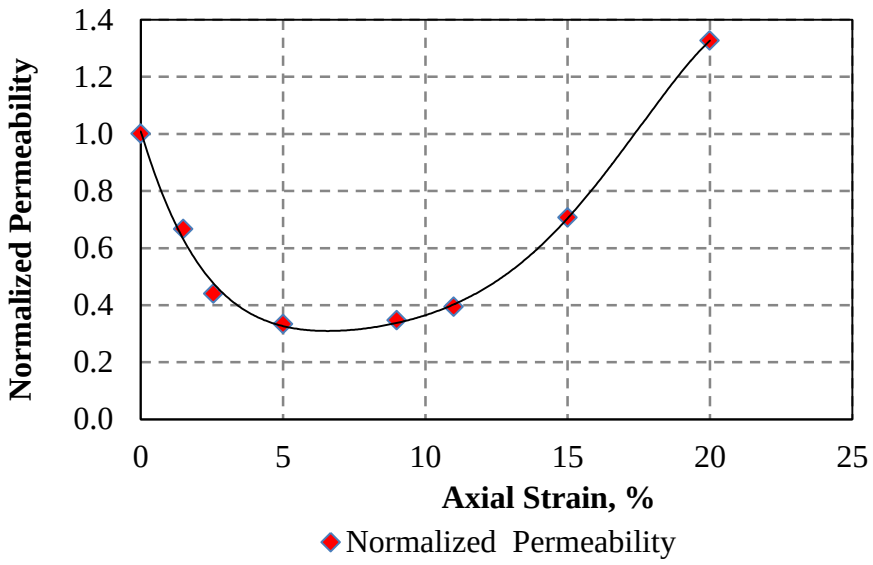

Figure 4.10: Normalized absolute permeability at different levels of axial strain at an effective confining stress of 600 kPa.

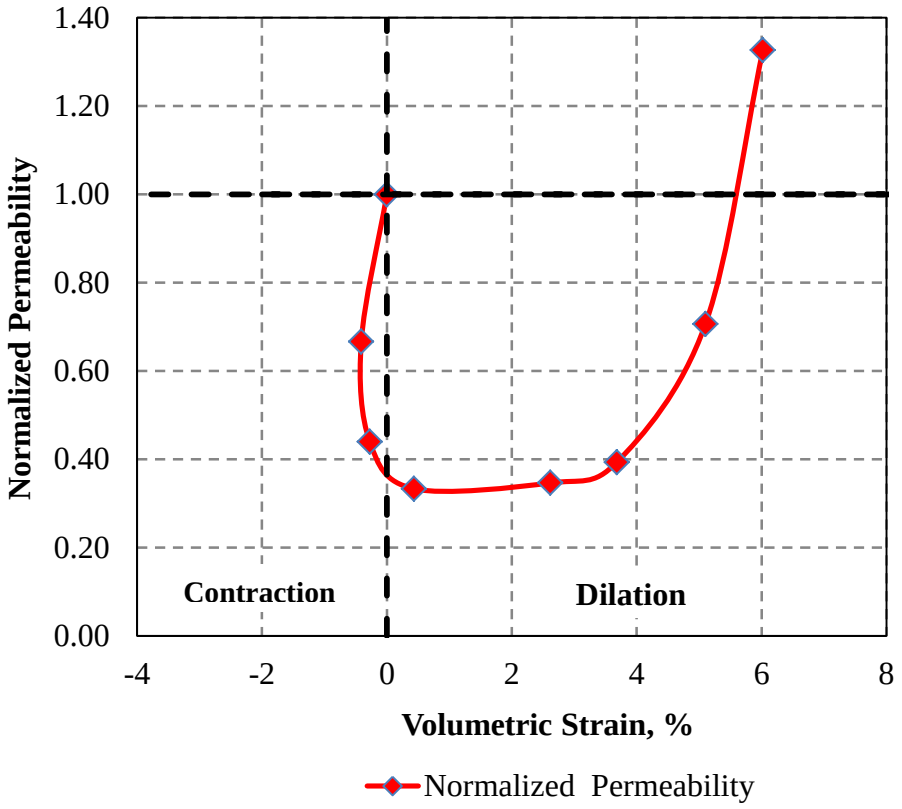

Figure 4.11: Normalized permeability-Volumetric strain relationship of specimen at an effective confining stress of 600 kPa.

4.6.1.3 Absolute Permeability-Volumetric Strain Relationship during Dilation

As noted in Figure 4.11, there is a large reduction in absolute permeability before shear induced dilation leads to increase in absolute permeability. Several researchers (Oldakowski 1994 and Touhidi-Baghini 1998) have examined the relationship between permeability and volumetric strain during shearing but in almost no cases is the initial reduction accounted for in these relationships. Most relationships

describing dilation-permeability change follow an exponential form with the most common equation to predict and develop relationships between permeability and porosity in sand packs of uniform size spheres being the Carman-Kozeny relationship; this is represented as follows (Equation 4.3)

$$k = C * \frac{\phi^a}{(1-\phi)^b} \quad \text{.....4.3}$$

where C is constant related to tortuosity, pore shape factor and grain size of sand, ϕ is porosity in fraction and k is permeability in cm^2 or μm^2. The constants ***a*** and ***b*** are determined experimentally. The combination of the Carman-Kozeny equation with the linear relationship between porosity and volumetric strain ($\phi = \frac{\varepsilon_V + \phi_{in}}{1+\varepsilon_V}$) results the following exponential form (Equation 4.4)

$$\frac{\boldsymbol{k}}{\mathbf{k_0}} = \boldsymbol{e^{C\varepsilon_V}} \quad \text{.....4.4}$$

where,

$C = [a*(1-\phi_0) + (\phi_0*b)]/ [\phi_0]$

in which,

$\frac{k}{k_0}$: Changes in permeability as function of volumetric strain;

C: Constant includes porosity at beginning of shearing and fitting parameters of a and b are determined from the experimental data; and

ε_v: Volumetric strain.

It is clear that the curve fit using the exponential equation (Equation 4.4) shown in Figure 4.12 fits the dilation part where the shear induced volume change is present; however, the compaction (contraction) portion is not covered by the exponential equation. This clearly identifies the need to find an equation that covers the full range of volumetric strain of the specimen and to capture the sensitivity of this relationship to effective confining stress. Figure 4.12 summarises the relation between permeability ratio and volumetric strain for uniform dense sand specimen.

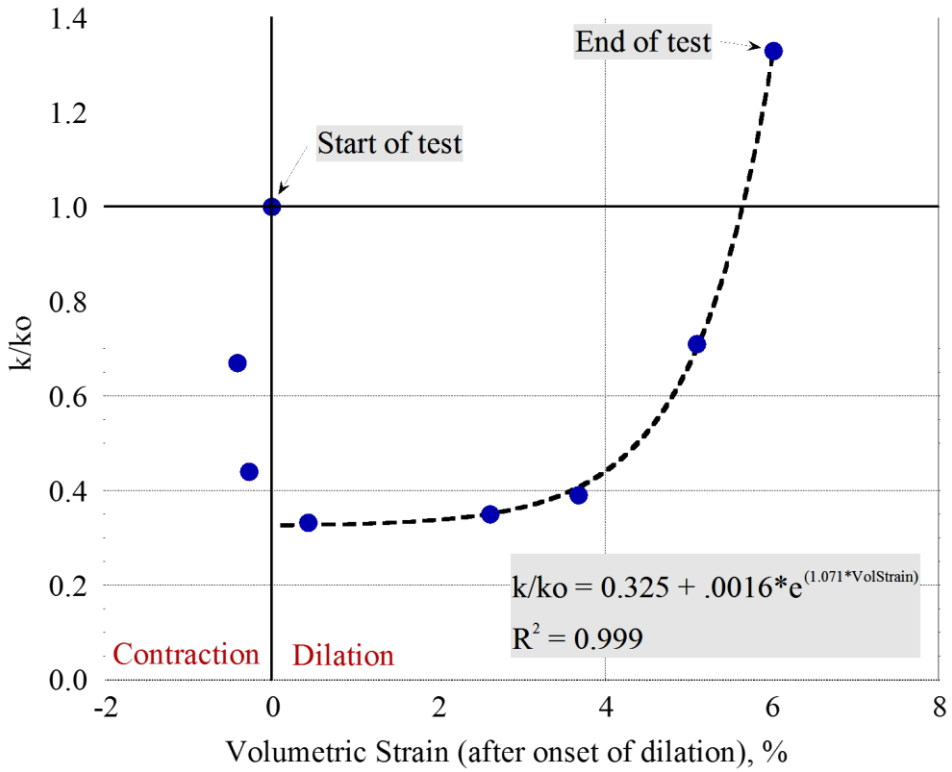

Figure 4.12 Correlation between permeability ratio and volumetric strain at an effective confining stress of 600 kPa.

4.6.2 Relative Permeability

Under two-phase flow conditions, the average irreducible water saturation during drained triaxial compression test (Figure 4.13) and from compaction to dilation stage ranged from 8 to 13 %, which is consistent with Polikar et al. (1988). The overall residual oil saturation, however, varied between 11-23 % (Figure 4.13).

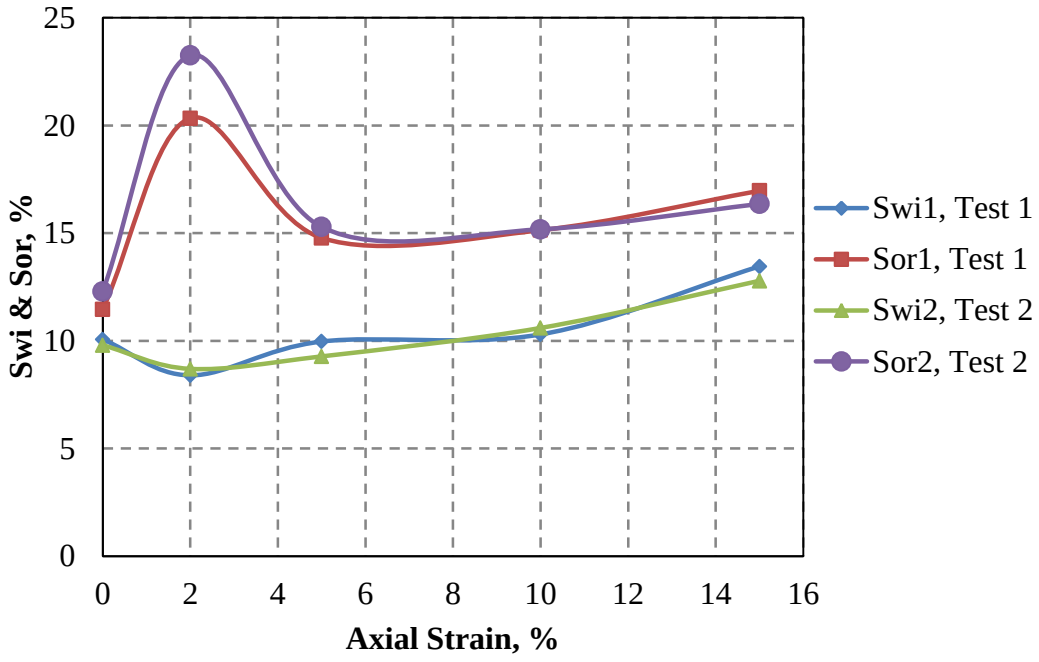

Figure 4.13: Irreducible water and residual oil saturation end points versus axial strain at an effective confining stress of 600kPa.

However, all oil relative permeability curves determined in this study, revealed convex shapes, as illustrated in Figure 4.14.

Encouragingly, in unconsolidated sands, Polikar (1988) came up with the same convex shape for uncemented sand.

4.6.2.1 Irreducible Water Saturation

Initially, the irreducible water declines from 10 % to attain 8.4 % at 2% of axial strain (Figure 4.13), and it increases again to its initial value at 5% of axial strain. This behaviour was also shown by Khan (2009). Eventually, when the axial strain reaches 10%, the irreducible water tends to flatten at 10%. Finally, at a critical stress state where there is no change in void ratio, the irreducible water remains relatively constant at 13.46 %.

4.6.2.2 Residual Oil Saturation

As can be clearly seen from Figure 4.13, the residual oil saturation increases during compaction and decreases during dilation and then increases again at the conclusion of the test. Indeed, the residual oil saturation begins to rise from 11.46 % to achieve peak value 20.34 % at 2 % of axial strain. After that, it increases to reach 14.78 % at 5% of axial strain, and then gradually increases to attain 16.97 % at 15 % of axial strain.

4.6.2.3 Oil/Water Relative Permeability

On the other hand, from Figure 4.14, the initial $k_{ro}(S_{wi})$ increases progressively from 0.729 at 0% axial strain to 0.888 and 0.932 at 2% and 5% of axial strain, respectively. In other words, the lower value of $k_{ro}(S_{wi})$ results pre-shearing and the higher value occurs at post shearing. However, for water relative permeability to residual oil ($k_{rw}(S_{or})$) (or end point) increases during compaction from 0.082 to 0.148, which corresponds to 0% and 2%, respectively of axial strain, then it decreases from 2% to 10% to reach 0.054, and it rises slightly to 0.072 at 15% of axial strain. It has also been observed that two-phase flow varied over a wide range prior to shearing of the specimen, but the range of results narrowed considerably following initial consolidation (compaction) of the specimens. These findings match those reported by Morgan et al. (1970). For the shearing stages, however, the range of results showed increasing variability, as shown in Figure 4.14. There is an increase of this range of results at 5% of axial strain and a gradual decrease from 10% to 15% of axial strain (Figure 4.14).

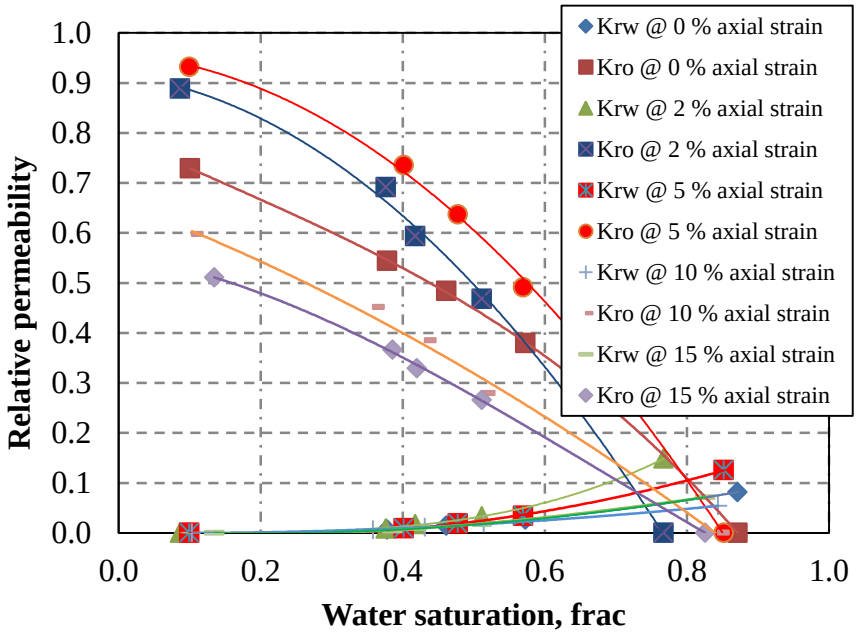

Figure 4.14: Sensitivity of relative permeability curves at different levels of axial strain and at an effective confining stress of 600 kPa.

4.6.2.4 Relative Permeability from Analytical Equation

For the future purpose of reservoir simulation, analytical equations (for instance, Brooks and Corey's model) are the most functional form that expresses relative permeability curves in numerical simulators. The experimental results plotted in Figure 4.14 are fitted with Equations 4.5 and 4.6:

Water relative permeability (Equation 4.5):

$$k_{rw} = k_{rw}(S_{or})\left(\frac{S_w - S_{wi}}{1 - S_{wi} - S_{or}}\right)^{n_w} \quad \ldots\ldots\ldots\ldots \quad 4.5$$

Oil relative permeability (Equation 4.6):

$$k_{ro} = k_{ro}(S_{wi})\left(\frac{1-S_w-S_{or}}{1-S_{wi}-S_{or}}\right)^{n_o} \quad \text{..... 4.6}$$

where,

$k_{rw}(S_{or})$: end point relative permeability to water at residual oil saturation

S_w: water saturation

S_{wi}: irreducible water saturation

S_{or}: residual oil saturation

$k_{ro}(S_{wi})$: end point relative permeability to oil at irreducible water saturation

n_o and n_w: Corey exponents for oil and water, respectively.

The least square regression method is used to estimate the parameters in the Corey model. The values of n_o and n_w are determined from the experimental results. Figures from A.8 to A.12 in the Appendix show that the Corey exponent to water (n_w) increases during compaction reaching a maximum value of 6 as compared to its initial value (n_w=2) and decreases to 2.5 during dilation, then stabilises at 1.8. Corey exponent to oil (n_o), however, varies only slightly from 0.6 to 0.7, respectively, during compaction to dilation.

4.6.2.5 Capillary Pressure and Hysteresis Effect due to Oilflood Cycle and Shearing

It has been observed from preliminary capillary pressure measurements that both cycles of drainage are significantly affected by the shearing stress. At the initial stress state, there is a slight hysteresis effect. However, at 5% of axial strain the level of hysteresis starts increasing, to reach its maximum at 10 % of axial strain. Then, there is an attenuation of hysteresis effect at 15 % of axial strain (Figure 4.15). It is clear that results from capillary pressure measurements show a significant hysteresis between the first and second cycle oilflood and this is due to cycle dependant hysteresis (Hawkins et al (1989)) and to stress change. Capillary pressure controls the initial fluid saturation distribution and therefore a small change in reservoir state can have significant impacts on reservoir performance.

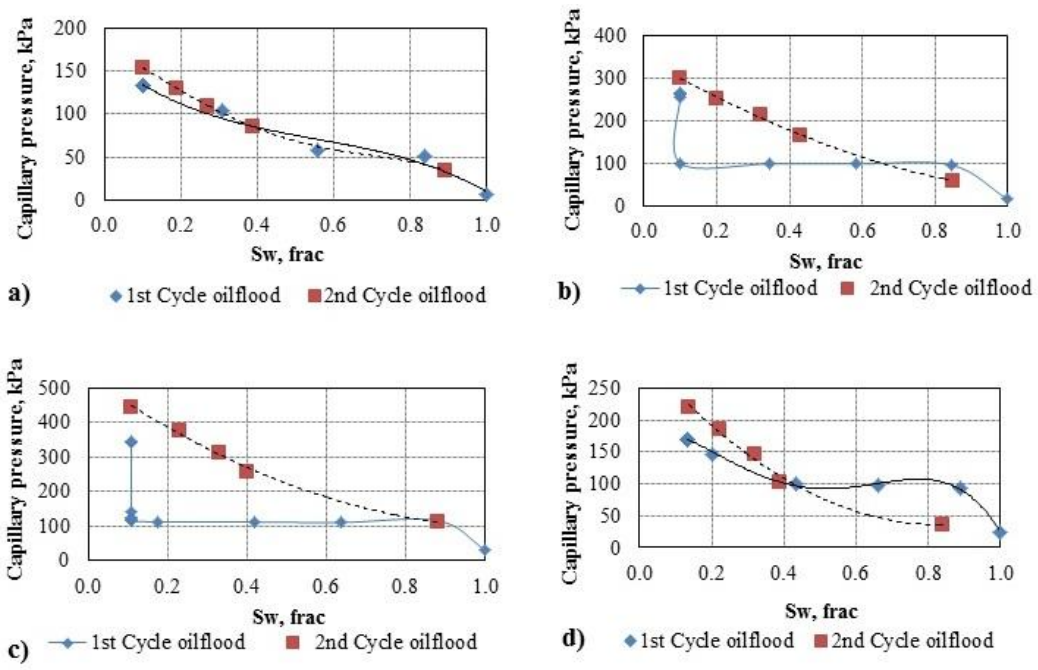

Figure 4.15: The impact of the shearing process on hysteresis during primary/secondary drainage at different levels of axial strain and at an effective confining stress of 600 kPa. a) Initial stress state; b) Shearing @ 5% of axial strain; c) Shearing @10% of axial strain; and d) shearing @ 15% of axial strain.

4.6.3 Discussion

Figures 4.16 and 4.17 illustrate the variation of end point saturations with volumetric strain and deviatoric stress, respectively. Morgan et al. (1970) state that pore geometry is the main parameter that affects relative permeability. As shown in Figures 4.16 and 4.17, the decrease of irreducible water from 10% to 8.4% resulted from a decrease in specimen volume (contraction). As the specimen contracted, the pore volume decreased resulting in water being displaced into larger voids where the displacing fluid (oil), which normally occupied these larger

pores, was displaced. In other words, smaller pores and throats, during drainage process, continue to fill with non-wetting phase and as pore space is getting smaller leads to an increase of capillary pressure, an increase in the volume of mobile water flowing out of the specimen and therefore, a decrease of irreducible water saturation.

Geomechanically speaking, this is explained by the contraction of the core sample, which results in water flowing out of the specimen and reduction in the volume of the specimen.

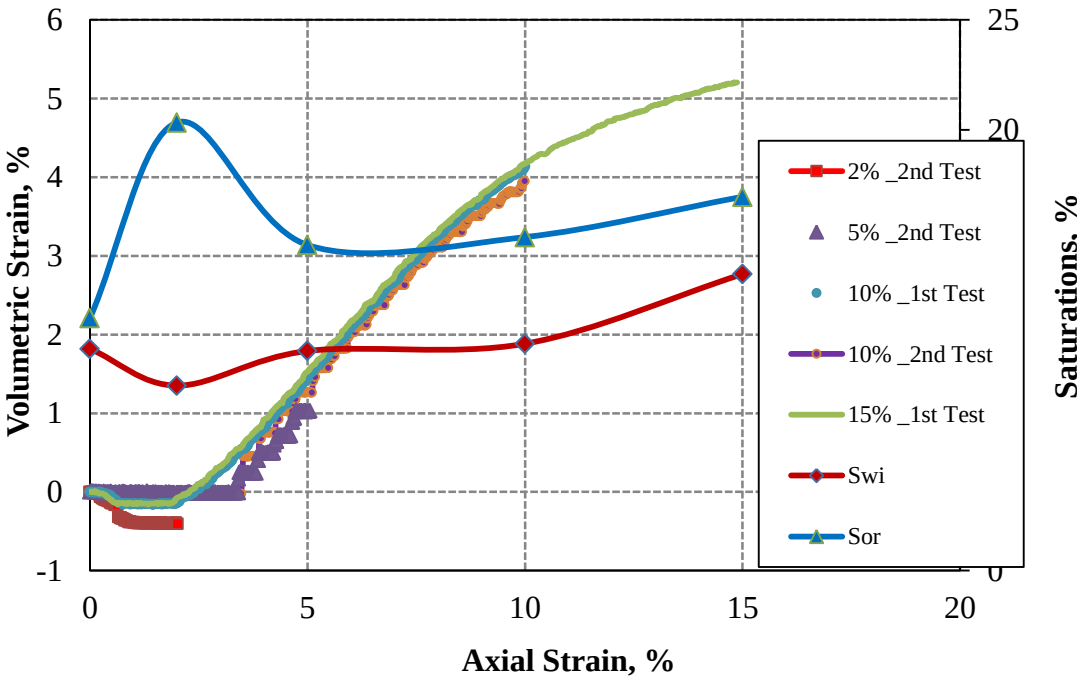

Figure 4.16: Volumetric strain and saturation end points at different levels of axial strain and at an effective confining stress 600kPa.

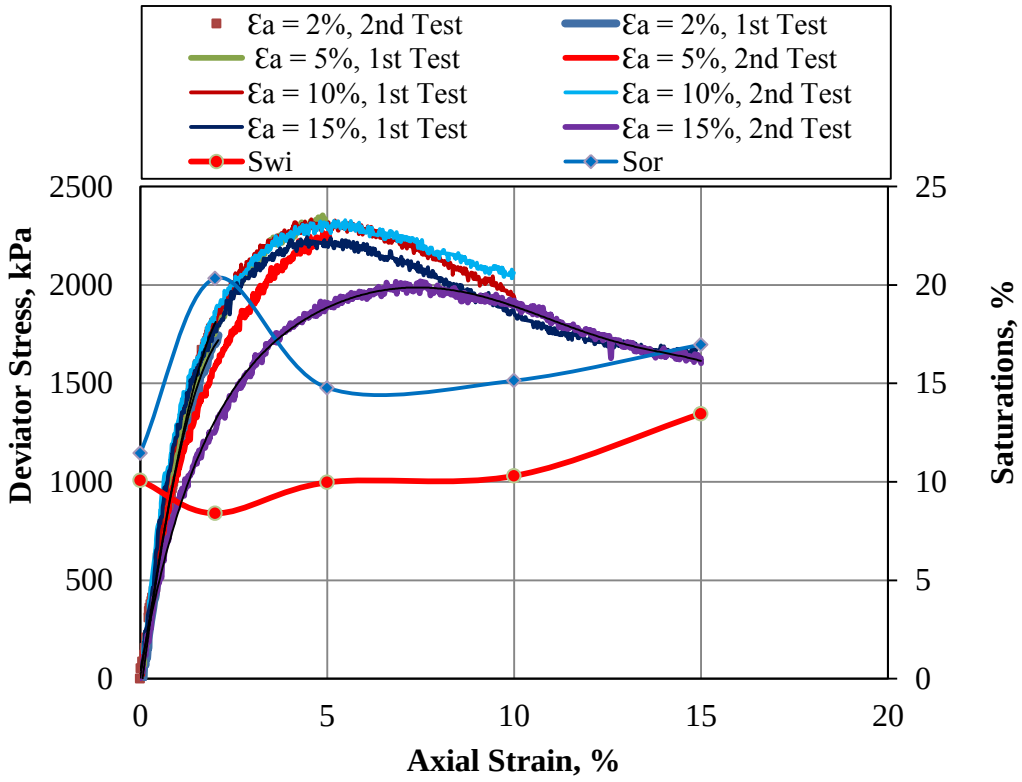

Figure 4.17: Deviatoric stress and saturation end points at different levels of axial strain and at an effective confining stress 600kPa.

At the onset of dilation at an axial strain of ~ 5%, the irreducible water saturation began to increase slightly, ending at a value just below its initial value of ~10.0%. As the deviator stress decreased towards the final post-peak stress value, the irreducible water rose to approximately 13.5%. The increase in S_{wi} was due to increase in pore surface area as a result of dilatant volume changes within the specimen. This behaviour was verified during the imbibition process where the capillary number was in the range of 10^{-6}, similar to a typical waterflood process. Under

such conditions, according to Foster (1973) and Melrose and Brander (1974), the capillary forces dominate the flow process.

Residual oil saturation, however, displays a more complex response to volumetric changes within the specimen, as shown in Figures 4.16 and 4.17. The residual oil saturation began to rise during initial compaction of the specimen, attaining a peak value 20.3% just as the volumetric behaviour transitions from compaction to dilation. At approximately the peak deviatoric stress (axial strain ~ 5%), S_{or} decreases to approximately 14.8 % and then displays a mild increase with increased straining reaching a final value of 17% at an axial strain of 15%. A similar increase/decrease in S_{or} with volumetric strain was also found by Khan (2009). It can be clearly seen that compaction has affected residual oil saturation and therefore the recovery factor (Figure 4.18). This was due mainly to snap-off effects when the droplets of oil are getting trapped into the pore space where the capillary pressure is less than that in the throat of the pore (less constriction). The pore volumes became smaller and consequently inhibited flow of the mobile fluid phase. In the first stage of dilation, where the failure caused increasing pore volumes, there was an improvement of residual oil saturation respective to large pore space in which there is a decrease of capillary pressure and therefore there is less restriction for trapping oil. Eventually, when the shearing reached its post-peak value at 15% axial strain, the flow path changed

and was likely influenced by the presence of a shear surface inclined to the axis of the specimen (as governed by its internal friction angle of approximately 33^{o}) and the tortuosity of porous medium would have definitely been altered. In addition, because of the boundary conditions within the triaxial test (Figure 4.19), the distribution of porosity changes within the specimen at this axial strain (15%) and are clearly not uniformly distributed. As shown in Figure 4.20, evidence from SEM analysis shows that the arrangement of grains after shearing tests, in both upper and bottom parts of the specimen, was more compacted than in the middle one. Within the compacted zone (adjacent to the specimen end platens), the capillary forces would dominate flow and would influence measurement of S_{or}. The development of these compacted regions was also evident in the results of differential pressure during different levels of strain and from the first cycle of oilflood, which showed that the displacement (entry) pressure increased gradually as axial strain rose (Figure 4.21), so the degree of pore closure was controlled by this entry pressure.

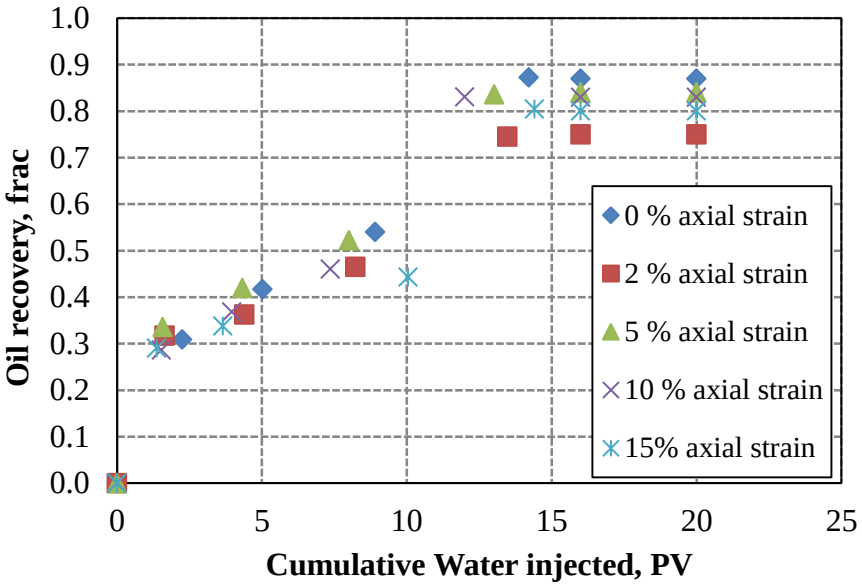

Figure 4.18: Oil recovery at different levels of axial strain and at an effective confining stress of 600kPa.

Figure 4.19: Effect of end platens on specimen at the end of shearing.

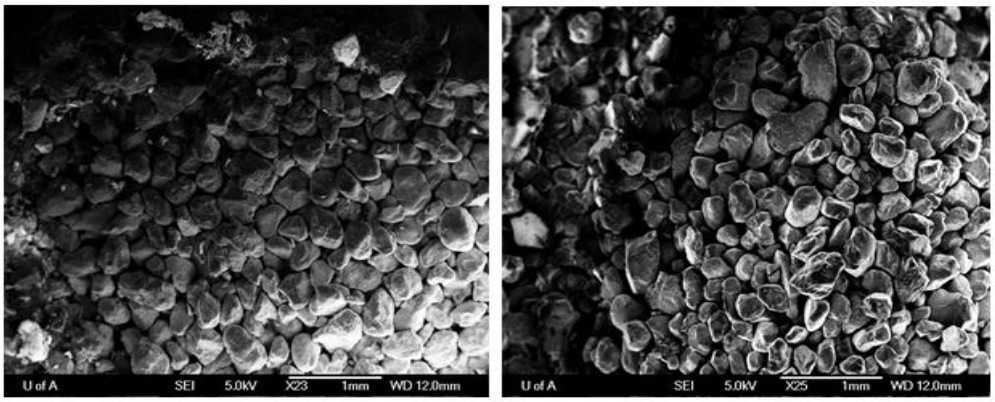

from left to right snapshot of top and bottom part of specimen

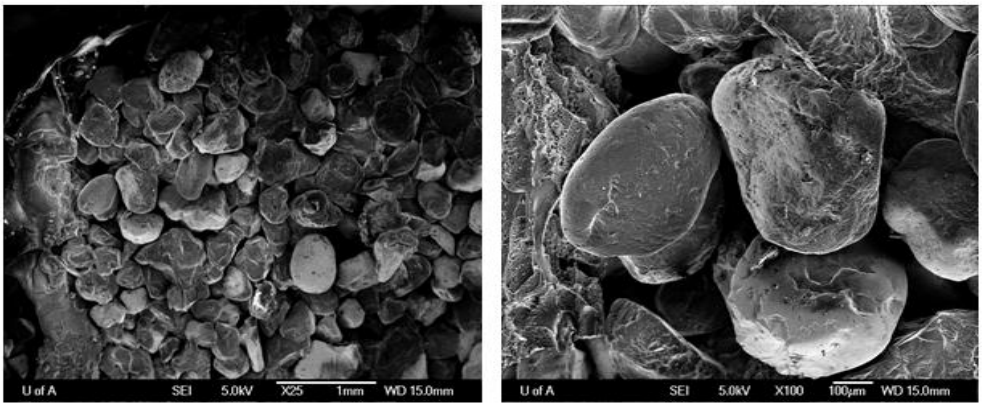

Snapshot of middle part of specimen

Figure 4.20: Snapshot of SEM analysis at top, bottom and middle part of specimen.

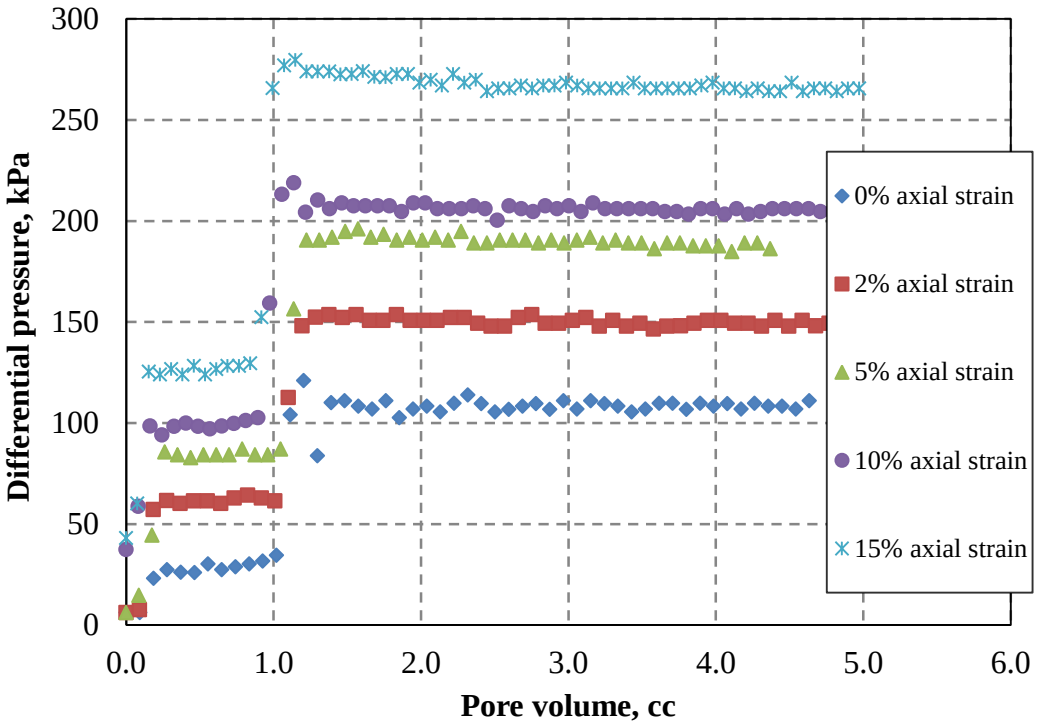

Figure 4.21: Differential pressure versus pore volume at different levels of axial strain.

Based on the above results, the residual oil saturation increased from 14.78 % to 16.97 % for axial strains of 10 % and 15 %, respectively.

Chapter 5 Conclusions and Recommendations

5.1 Conclusions

The following summarises the conclusions from this research:

- The most important links between reservoir engineering and the reservoir geomechanics is the porosity of porous media;
- The results generated in this work support the belief that rock properties such as porosity and permeability change significantly in unconsolidated and shallow reservoirs during stress change;
- The analytical Kozeny-Carman equation provides a reasonable prediction of the initial absolute permeability of reconstituted sand specimens;
- It has been shown that the permeability-volumetric strain relationships shear induced volume change follow an exponential form however the permeability reduction, during contraction, is not accounted for by the same exponential equation;
- Irreducible water saturation, S_{wi}, decreased during contraction followed by a moderate increase during the shear-induced dilatant volumetric strain with the specimens;
- Changes in S_{or}, the residual oil saturation, displayed a complex behaviour, controlled by shear induced volumetric changes within the specimen. S_{or} increased during initial contraction of the specimen but

decreased quickly following the onset of dilatant volume changes;

- Despite of the concave shape of the oil relative permeability curves in conventional oil reservoirs, the steady state measurements in unconsolidated sands yielded convex oil relative permeability curves;
- The endpoint oil relative permeability was more sensitive to shear induced volume changes than the endpoint water relative permeability. For contractant volume changes, k_{ro} endpoints increased by 21.8% whereas k_{rw} endpoints exhibited a large change of 42.6%. At large volumetric strains, k_{ro} endpoints decreased by 30% below its initial volume while k_{rw} displayed a small change of 12%;
- All relative permeability curves exhibited, at $k_{ro} = k_{rw}$, water saturations above 50%. Therefore, they follow Craig's wettability criteria, which indicates strongly water wet conditions;
- Two-phase flow existed over a narrow range during compaction, and over a wide range variation during dilation; this means residual saturations are higher during compaction and lower during dilation.
- For reservoir simulation purposes, analytical relative permeability relationships such as Corey's model can be used to represent each set of relative permeability curves at each strain level;
- Results from capillary pressure measurements show a significant effect due to cycle-dependent hysteresis and to stress change; and

- The results from this research provide clear evidence that geomechanical processes that influence pore geometry, such as shear induced volume changes, may exert a significant effect on two-phase flow recovery.

5.2 Recommendations

Recommendations for future research are:

- Testing should be extended to study the influence of different effective confining stresses;
- For future studies relative permeability tests should be conducted at true reservoir pore pressure;
- Accurate in situ techniques such as X-ray or CT scans should be used for saturation determination;
- Duplication of this study on an unsteady state should be considered to compare with the steady state technique;
- Application on a bitumen/steam system is recommended;
- The behaviour of two-phase flow such as gas storage in shallow reservoirs has to be investigated on a gas/oil system;
- The impact of results of this study should be projected and investigated in full field model reservoir simulation; and
- Extreme care should be taken to avoid desiccation (freeze drying) occurring in frozen specimens as it creates difficulties in achieving

saturation with the specimens when operating at low pore pressures.

References

Ali, H.S., Al-Marhoun, M.A., Abu-Kahmsin, S.A., and Celik, M.S., 1987. The Effect of Overburden Pressure on Relative Permeability. Society of Petroleum and Engineering. SPE paper 1573.

Ahmed, T. 2000. Reservoir Engineering. Handbook, United States: Gulf Professional Publishing. ISBN 0-88415-776-8.

Arora, K.R., 2005. Soil Mechanics and Foundation Engineering. Handbook. Lomus Offset Press, Delhi. ISBN 81-8014-028-8.

Bishop, A.W., and Henkel, D.J., 1962. The Measurement of Soil Properties in the Triaxial Test. Spottiswoode Ballantyne Ltd., Colchester and London. ISBN 0 7131 3004 0.

Budhu, M. 2007. Soil Mechanics and Foundations. John Willey & sons, Inc., New Jersey, USA.

Chalaturnyk, R. 1996. Geomechanics of the Steam Assisted Gravity Drainage Process in Heavy Oil Reservoirs. Ph.D. thesis, the University of Alberta.

Craig, F.F., 1971. The Reservoir Engineering Aspects of Water Flooding. Monograph Series, Vol. 3, Society of Petroleum Engineers of AIME, Dallas, Texas, USA.

Das, B.M., 2000. Fundamentals of Geotechnical Engineering. Handbook, Brooks/Cole, USA. ISBN 0-534-37114-0.

Dobrynin, V.M., 1962. Effect of Overburden Pressure on some Properties of Sandstones. Society of Petroleum Journal 465, Vol.2, pp.2.

Fatt, I., and Davis, D.H., 1952. Reduction in Permeability with Overburden Pressure. Petroleum Transactions, AIME, Vol.4. pp. 12.

Fatt, I., 1953. The Effect of Overburden Pressure on Relative Permeability. Journal of the American Institute of Mechanical Engineers, Petroleum Transactions, Vol. 198. Pp. 325-326.

Foster, W.R., 1973. A Low-Tension Waterflooding Process. Journal Petroleum Technology. SPE 3803, Vol. 25, pp. 2.

Gray, D.H., Fatt. I., and Bergamini, G., 1963. The Effect of Stress on Permeability of Sandstone Cores. Society of Petroleum and Engineering Journal. SPE 531, Vol.3 pp. 2.

Hamoud, M., R.J. Chalaturnyk and J. Leung. 2012. Influence of Geomechanical Processes on Relative Permeability. Canadian Rock Mechanics Symposium, Edmonton, Alberta, May 5-9.

Hawkins, T.J., and Bouchard, A.J., 1989. Reservoir Engineering Implications of Capillary Pressure and Relative Permeability Hysteresis. Special Core analysis Conference. SCA 8909.

Head, K.H., 1986. Manual of soil laboratory testing, Vol.3. Halsted Press, a Division of John Wiley & sons, Inc., New York. ISBN 0-470-20236-X.

Honarpour, M., Koederitz, L. and Harvey, A.H., 1994. Relative Permeability of Petroleum Reservoirs. Handbook, United States. ISBN 1-55563-063-4.

Jones, C., Al-Quraishi, A.A., Somerville, J.M., and Hamilton, S.A. 2001. Stress Sensitivity of Saturation and End–Point Relative Permeabilities. International Symposium of Society of core analysts, Edinburgh, Scotland, 17-29 September.

Jones, C., and Smart, B.G.D., 2002. Stress Induced in Two-Phase Permeability. Society of Petroleum and Engineering. Rock Mechanics Conference, Irving, Texas, USA, 20-23 October, SPE 78155.

Khan, H.A., 2009. Shear Induced Relative Permeability Change in Uncemented Sands. MSc. Thesis, the University of Texas at Austin, USA.

Lambe, T.W. and Whitman, R.V., 2000. Soil Mechanics, series in Soil Engineering. India. John Wiley & sons (Asia) Pte Ltd. ISBN 9971-513-17-X.

Manual of Artificial Oil Sand Sample Preparation, 2001. Geotechnical Group, Department of Civil & Environmental Engineering, University of Alberta.

Morgan, J.T. and Gordan, D.T., 1970. Influence of Pore Geometry on Water-Oil Relative Permeability. Journal Petroleum Technology, October, pp. 1199-1208

Melorose, J.C. and Brander, C.F., 1974. Role of Capillary Forces in Determining Microscopic Displacement Efficiency for Oil Recovery by Waterflooding. The Journal of Canadian Petroleum. SPE 74-04-05, vol. 13, pp. 4.

Marek, B.F., 1979. Permeability Loss in Depletion of Reservoirs. Society of Petroleum and Engineering. SPE Annual Technical Conference and Exhibition, 23-26 September, Las Vegas, Nevada. SPE 8433.

Oldakowski, K., 1994. Stress Induced Permeability Changes of Athabasca Oil Sands. MSc. thesis, the University of Alberta.

Polikar, M., Puttagunta, V.R., Ferracuti, F. and Farouq Ali, S.M., 1988. Journal of Petroleum Science and Engineering, p. 263-270.s.

Poulos, H.G. and Davis, E.H., 1974, 411pp. Elastic Solutions for Soil and Rock Mechanics.

Rapoport, L.A. and Leas, W.J., 1953. Properties of Linear Waterflood. Trans. AIME, 198, p.139-148.

Scott, J.D., Adhikary, D. and Proskin, S.A., 1991. Volume and Permeability Changes Associated with Steam Stimulation in Oil Sands Reservoirs. Petroleum Society of CIM and AOSTRA Technical Conference.

Stiles, J., June24-26, 2002. Using Special Core analysis in Reservoir Engineering, Wettability, Relative Permeability, and Residual Oil Saturation, Course Programme, Imperial College, UK.

Touhidi-Baghini, A., 1998. Absolute Permeability of McMurray Formation Oil Sands at Low Confining Stresses. Ph.D. thesis, the University of Alberta.

Tortike, S.W., 1991. Numerical Simulation of Thermal, Multiphase Fluid Flow In An Elastoplastic Deforming Oil Reservoir. Ph.D. thesis, the University of Alberta.

Towson, D.E. and Boberg, T.C., 1967. Gravity Drainage in Thermally Stimulated Wells. Proc. 18th Annual Technology Meeting. Petroleum Society of CIM, Banff.6p.

Tiab, D. and Donaldson, E.C. 1996. Theory and Practice of Measuring Reservoir Rock and Fluid Transport Properties. Handbook, United States: Gulf Professional Publishing. ISBN 0-88415-634-6.

Terzaghi, K. 1943. Theory of Elasticity. New York City: McGraw-Hill Book Company.

Yaich, E., 2008. The Effect of Shear Stress Paths and Shear Failure on the Permeability of Unconsolidated Sands. MSc. Thesis, the University of Texas at Austin, USA.

Appendix

Table A.1: B value of the majority of specimens

Core ID	Bi-Value
ID2_260811	0.89
ID3_260811	0.89
ID4_260811	0.88
ID5_290811	0.90
ID6_290811	0.90
ID7_290811	0.92
ID8_290811	0.93
ID9_290811	0.89
ID10_290811	0.92
ID11_310811	0.87
ID13_310811	0.88
ID14_310811	0.86
ID15_310811	0.90
ID16_310811	0.87
ID18_010911	0.86
ID19_010911	0.87
ID21_010911	0.92
ID22_120911	0.93

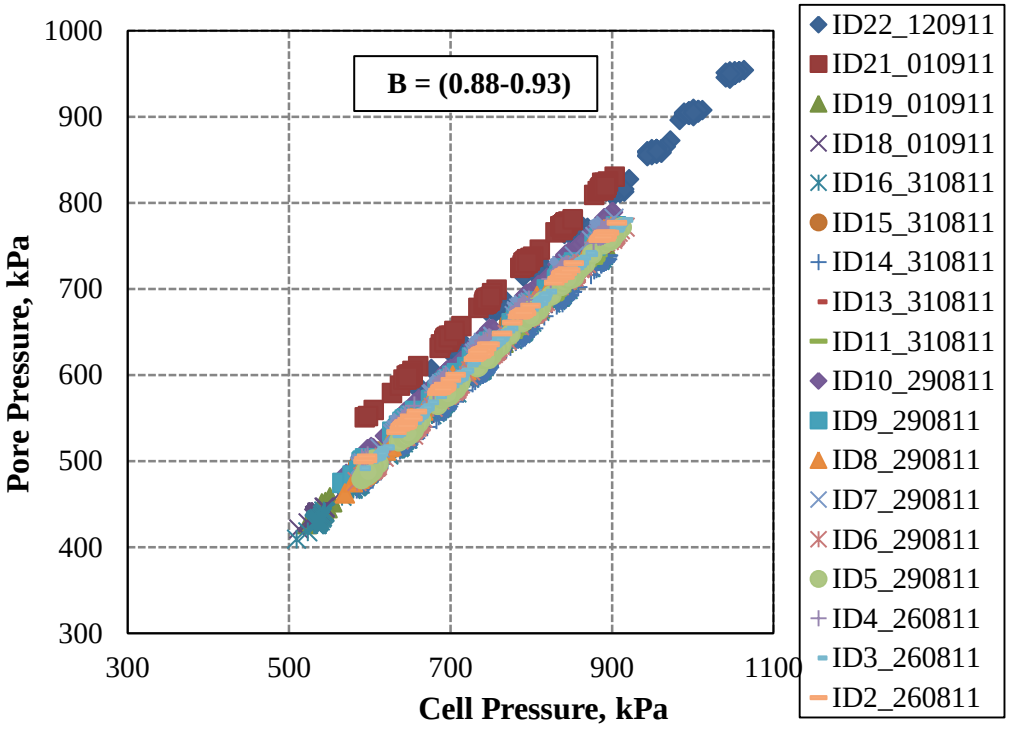

Figure A.1: Graphical representation of the majority of core samples during B Test.

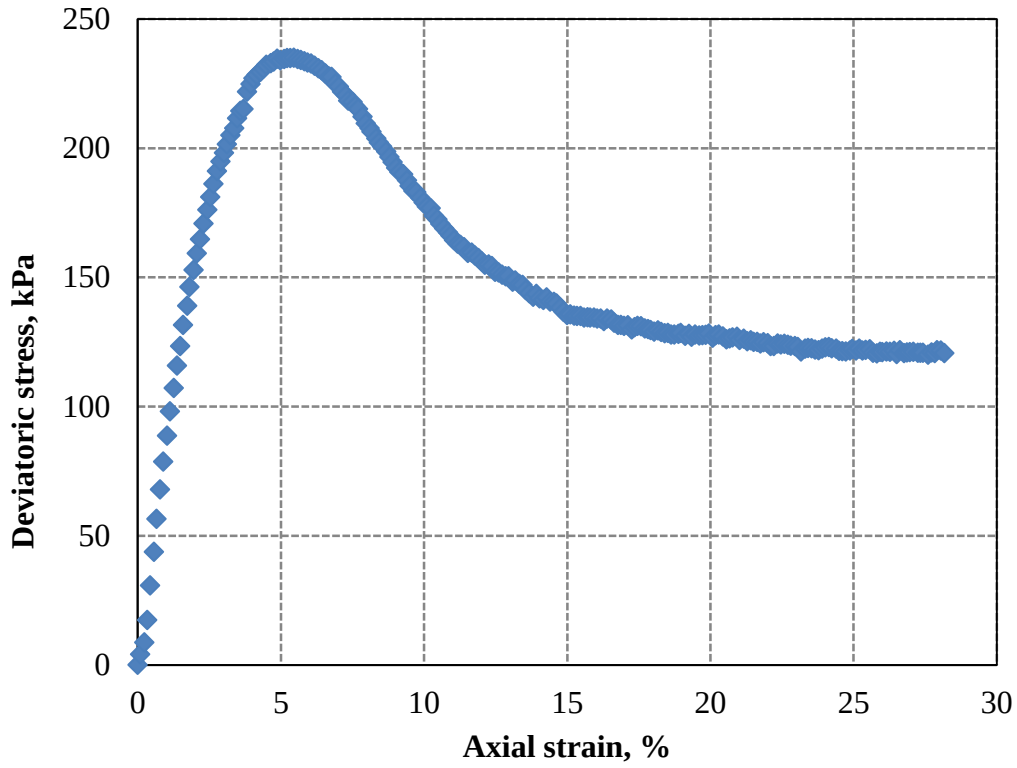

Figure A.2: Stress-strain for drained test of specimen at an effective confining stress of 50kPa.

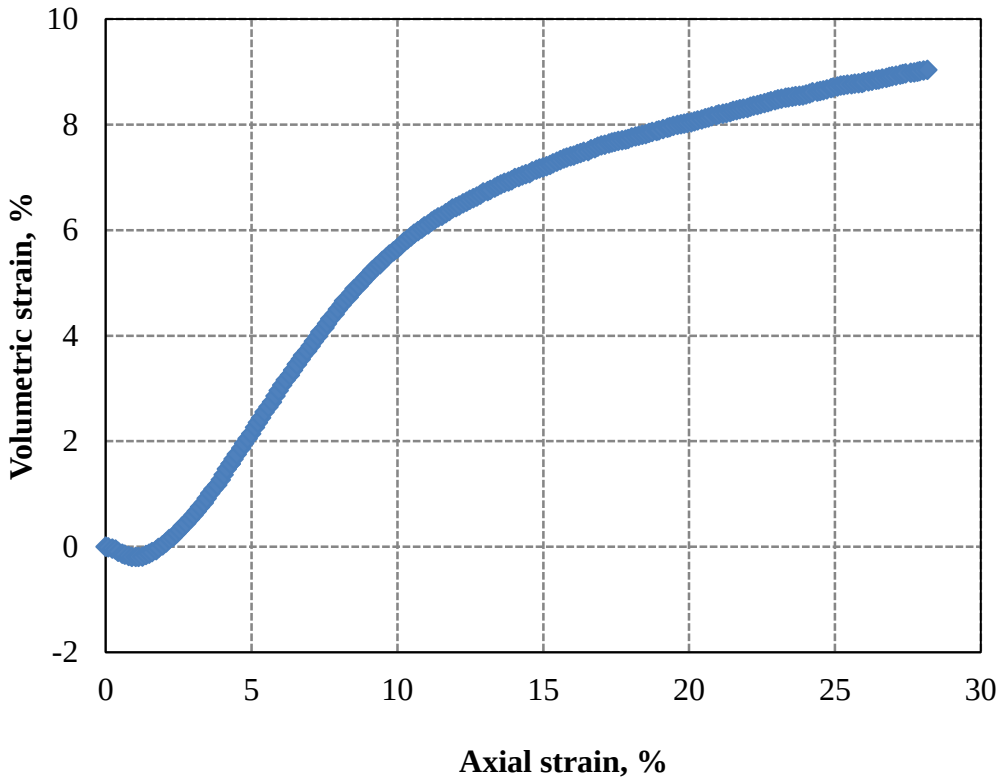

Figure A.3: Volumetric strain for drained test of specimen at an effective confining stress of 50kPa.

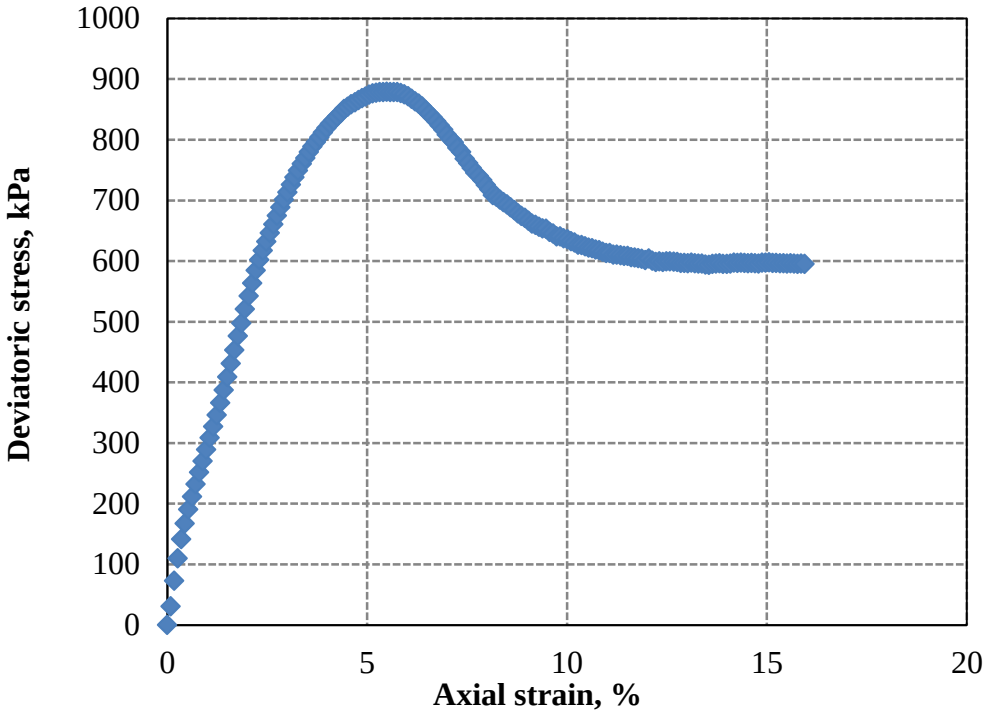

Figure A.4: Stress-strain for drained test of specimen at an effective confining stress of 200kPa.

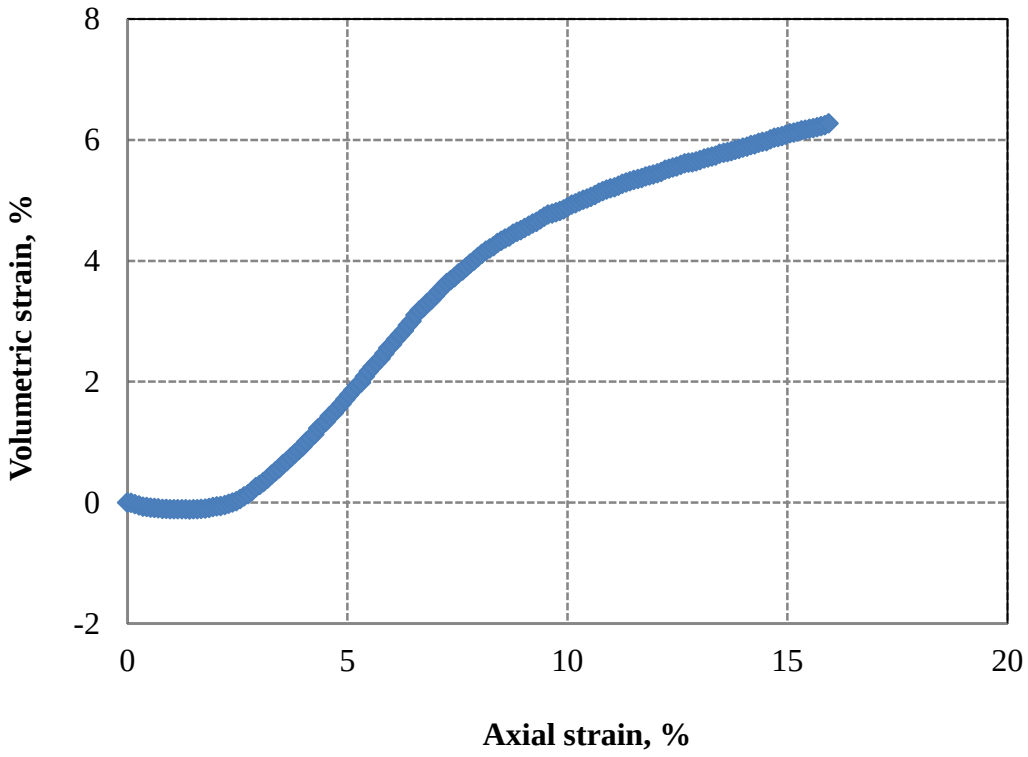

Figure A.5: Volumetric strain for drained test of specimen at an effective confining stress of 200kPa.

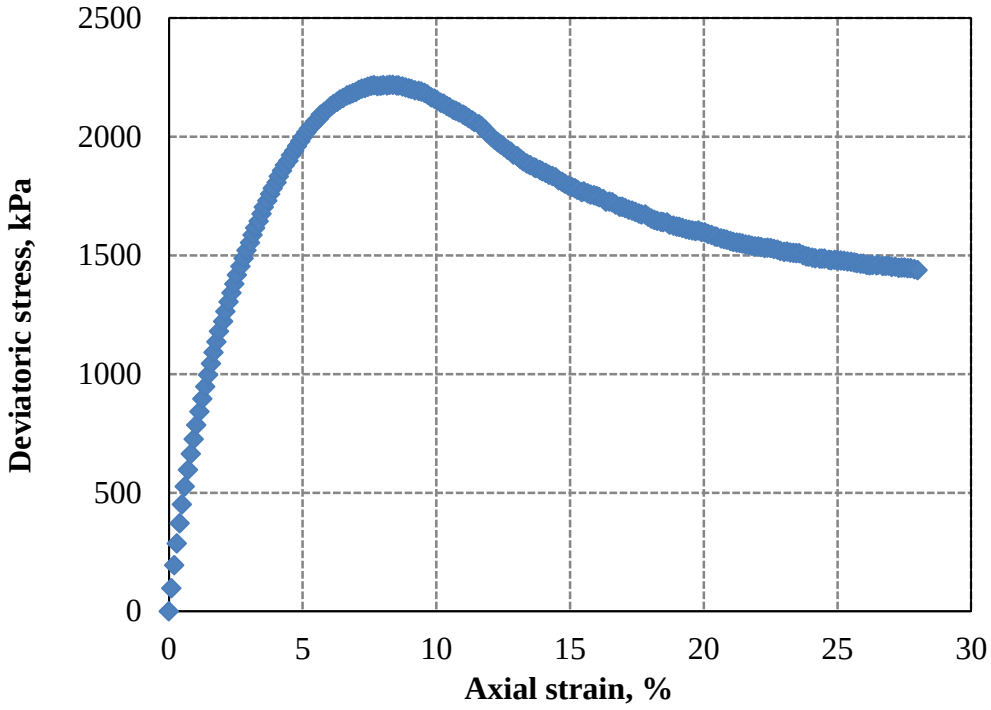

Figure A.6: Stress-strain for drained test of specimen at an effective confining stress of 600kPa.

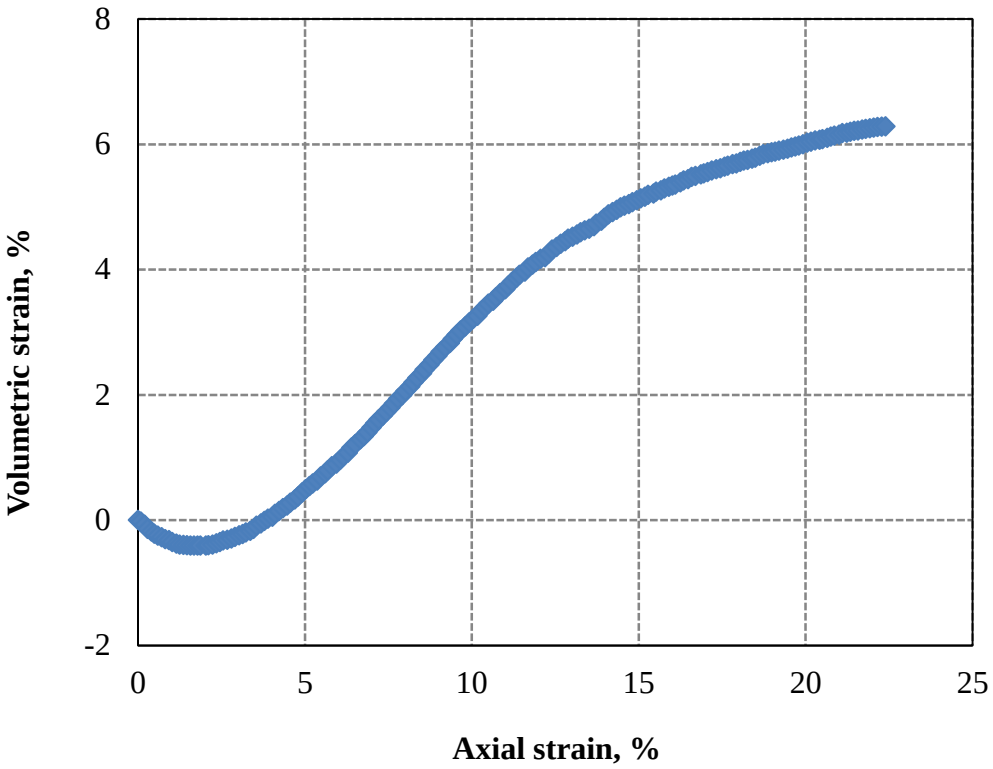

Figure A.7: Volumetric strain for drained test of specimen at an effective confining stress of 600kPa.

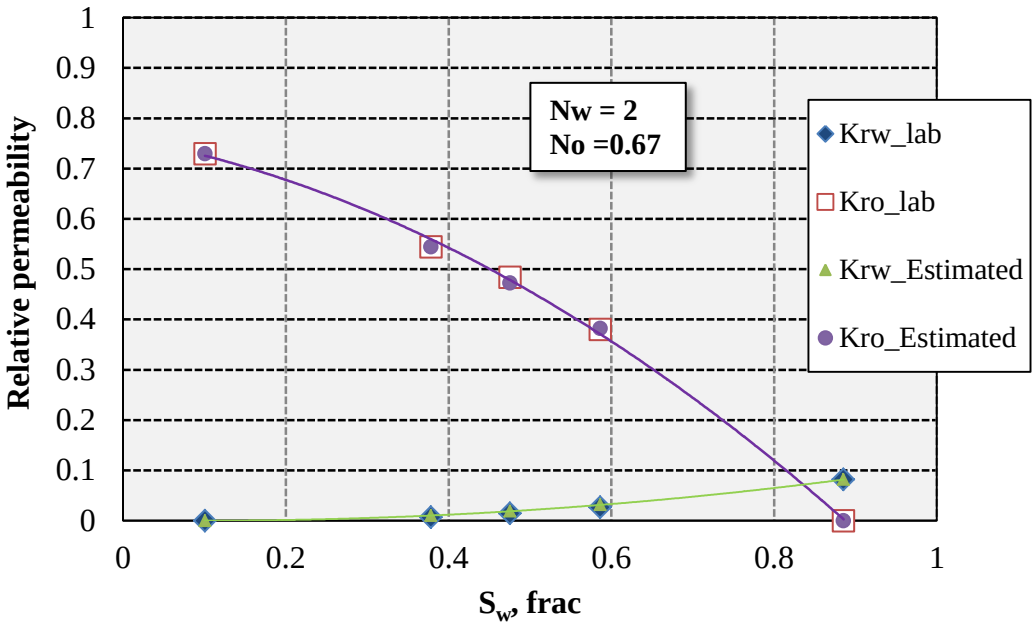

Figure A.8: Constructing relative permeability at initial stress state by fitting Corey's exponents.

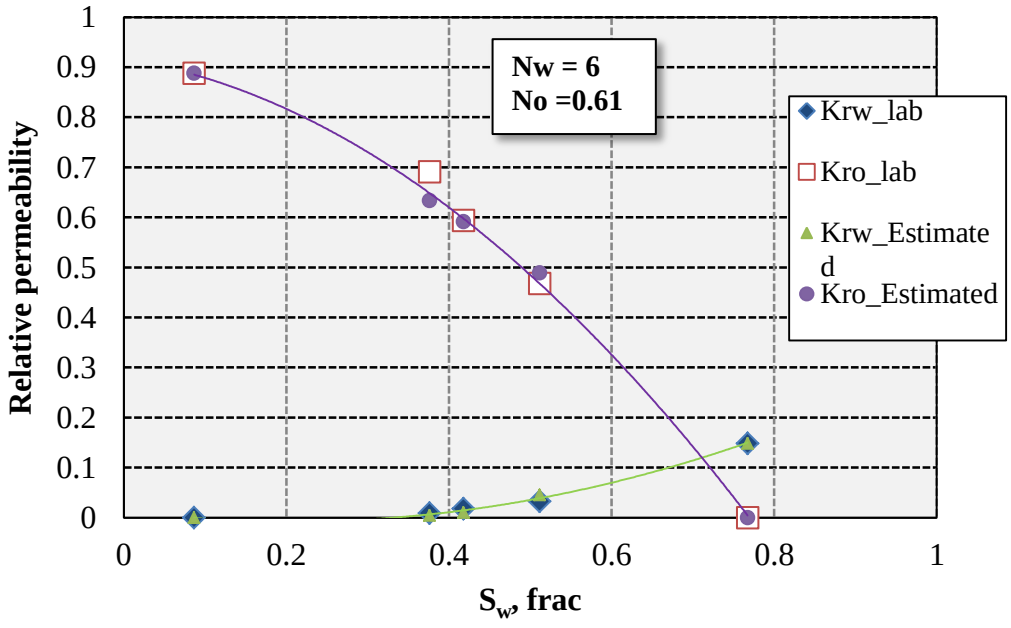

Figure A.9: Constructing relative permeability at 2% of axial strain by fitting Corey's exponents.

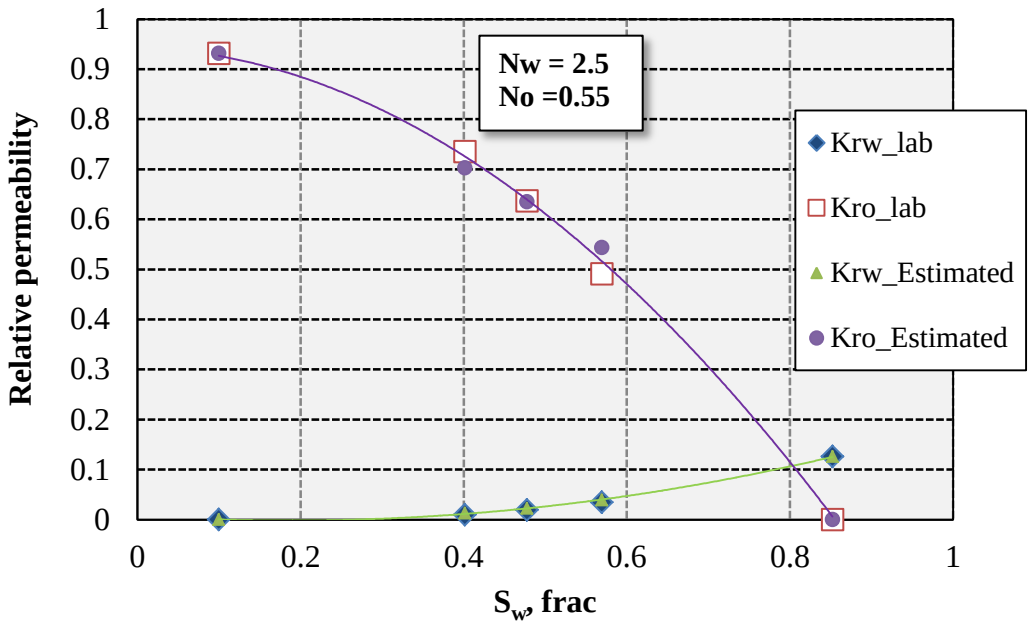

Figure A.10: Constructing relative permeability at 5% of axial strain by fitting Corey's exponents.

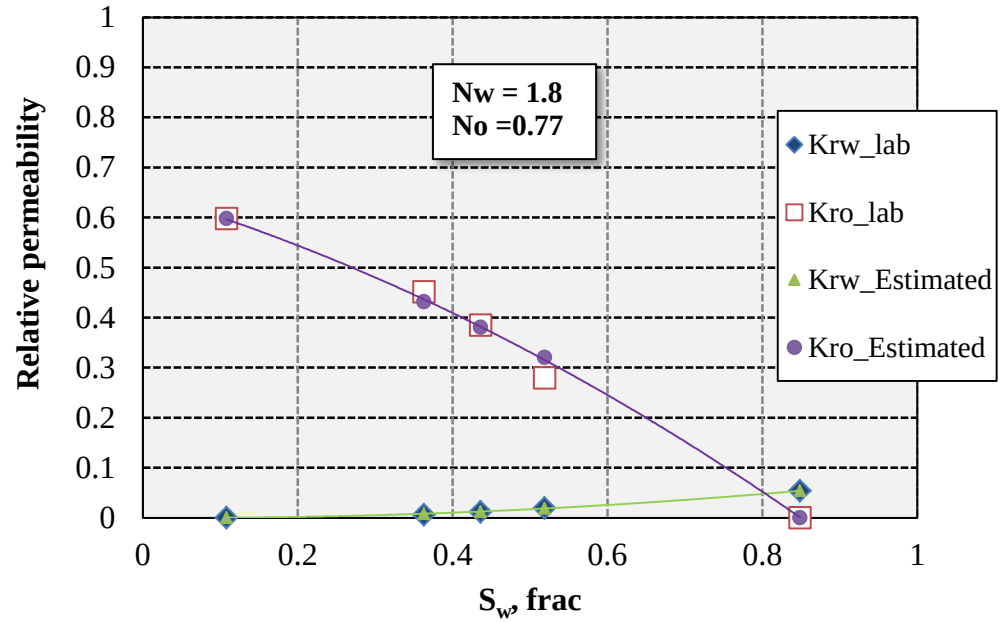

Figure A.11: Constructing relative permeability at 10% of axial strain by fitting Corey's exponents.

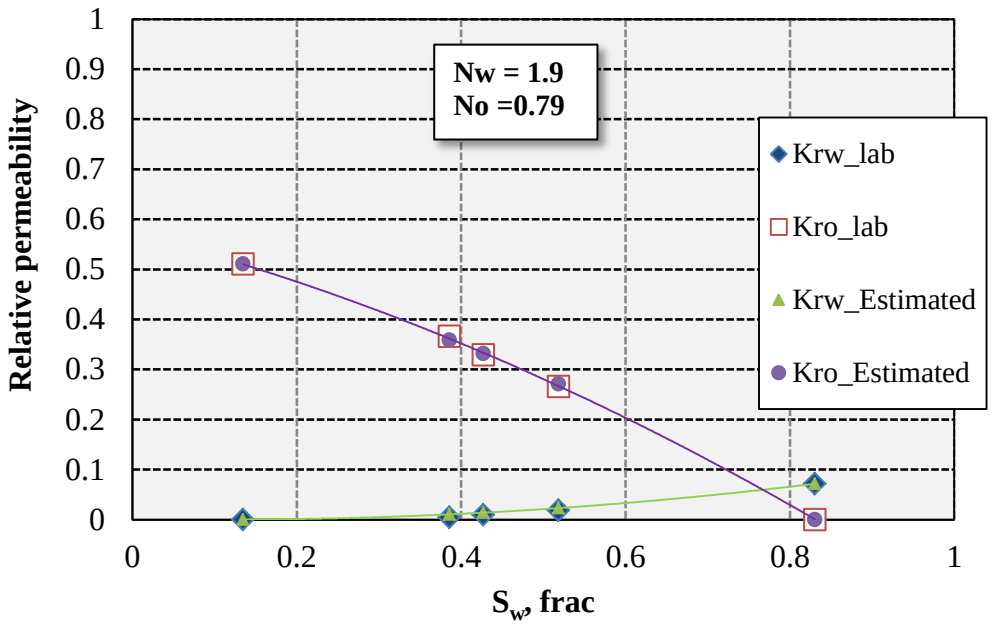

Figure A.12: Constructing relative permeability at 15% of axial strain by fitting Corey's exponents.